6-2021

Design and Fabrication of Zinc Oxide Optofluidic Laser Elements

Kyle T. Bodily

DESIGN AND FABRICATION OF ZINC OXIDE OPTOFLUIDIC LASER ELEMENTS

THESIS

Kyle T. Bodily, Captain, USSF

AFIT-ENG-MS-21-J-004

DEPARTMENT OF THE AIR FORCE
AIR UNIVERSITY

AIR FORCE INSTITUTE OF TECHNOLOGY

Wright-Patterson Air Force Base, Ohio

AFIT-ENG-MS-21-J-004

DESIGN AND FABRICATION OF ZINC OXIDE OPTOFLUIDIC LASER ELEMENTS

THESIS

Presented to the Faculty

Department of Electrical and Computer Engineering

Graduate School of Engineering and Management

Air Force Institute of Technology

Air University

Air Education and Training Command

In Partial Fulfillment of the Requirements for the

Degree of Master of Science in Electrical Engineering

Kyle T. Bodily, B.S.E.E

Captain, USSF

June 17 2021

AFIT-ENG-MS-21-J-004

DESIGN AND FABRICATION OF ZINC OXIDE OPTOFLUIDIC LASER ELEMENTS

Kyle T. Bodily, B.S.E.E

Captain, USSF

Committee Membership:

Dr. Hengky Chandrahalim
Chair

Dr. Michael A. Marciniak
Member

Dr. Anthony L. Franz
Member

Dr. Kevin Leedy
Member

AFIT-ENG-MS-21-J-004

Abstract

Sensing and signal processing with a coherent ultraviolet (UV) light source is of great interest for many applications. One material that has shown promise as a UV coherent light source is zinc oxide (ZnO) with its wide band gap and interesting optical properties. It is also of great interest to make these devices small and light and use low power. One way to accomplish this is through whispering gallery mode (WGM) optical resonators. WGM resonators have shown to be very attractive in lasing applications because of their high quality factor even when fabricated on a chip. Coupling two resonators for single mode emission, which is necessary for many sensing applications, is possible through the Vernier affect. This coupling is greatly enhanced using optofluidics. This thesis systematically goes through the derivation, simulation, and experimentation of Zinc Oxide optofluidic micro laser elements. Single and coupled ring resonators were simulated to show single mode transmission as well as enhanced coupling capabilities when surrounded by high refractive index liquid. Devices with diameters ranging from 100 – 500 μm were successfully fabricated inexpensively through standard cleanroom procedures. The devices were tested using two different pump laser systems. Testing included such factors as high pump intensity, various angles of excitation, and low temperature. In all cases photoluminescent emission was observed and recorded. A higher power laser is needed to see laser emission from the WGM resonators. Once laser emission is seen, then the optofluidic platform could be tested.

Acknowledgments

I would like to express my sincere appreciation to my faculty advisor, Dr. Hengky Chandralim, for his guidance and support throughout the course of this thesis effort. His insight and expertise were certainly appreciated. This thesis would not be possible without him. I would also like to express appreciation for the support of ARFL/RYD including Mr. Wally Rice, Mr. Timothy Prusnick, Dr. David Tomich, and Dr. John Cetnar. Their support and expertise were vital to the success of this thesis. I would like to thank each of my committee members, Dr. Michael Marciniak, Dr. Anthony Franz, and Dr. Kevin Leedy, for their time, talents, and expertise. I would also like thank the AFIT clean room technicians Mr. Rich Johnston and Mr. Adam Fritzsche.

Kyle T. Bodily

Table of Contents

Page

List of Figures

Page

List of Tables

Page

Design and Fabrication of Zinc Oxide Optofluidic Laser Elements

I. Introduction

1.1 Motivation

Sensors are an integral part modern technology. They are used in a variety of mechanical and electrical systems to give near instantaneous feedback on the performance and health of the system. However, like most parts of modern technology, the push is to make sensors smaller while keeping the same performance or even increasing the performance. This has been possible through the breakthroughs in micro fabrication of semiconductor devices. This allows for robust micrometer, or even nanometer, scale devices to be added into systems without significant impact to overall system weight or power consumption. This can bring great benefit to many defense systems as they continue to get more efficient.

An important subset of sensors is those that use a light source to gather and interpret information. These optical sensors can be designed to use any wavelength of light, but one area of great importance is having an ultraviolet (UV) coherent light source. Because of their shorter wavelength, UV sources can do more than long wavelength lasers. A UV source is needed for UV spectroscopy [1], meteorology [2], [3], optical signal processing [4], and various other sensing applications. UV light sources are highly desirable because their short wavelength and high energy allow for higher resolution.

The focus of this study will be on the fabrication and testing of microscale Whispering Gallery Mode (WGM) lasers that can be integrated into many sensing applications. The term Whispering Gallery was used by Lord Rayleigh in the early 1900s

to explain the phenomenon on sound waves being continuously propagated around the curved dome of St. Paul's Cathedral in London [5]. As will be discussed in Chapter II, it was later found that the same phenomenon applied to light that could be coupled into circular or spherical geometries of optical material through total internal reflection. This study will focus on fabricating and testing ring and disk geometries of WGM resonators made from zinc oxide (ZnO). The reason for choosing these structures and materials will be discussed further in Chapter II. Of particular interest in this study is the coupling of two of these devices, either two rings or two discs, through optofluidics. This thesis aims to study the possibility of generating a single-mode emission by evanescently coupling multiple WGM cavities. Liquids with high refractive indices will be dynamically used to enhance the evanescent coupling between WGM cavities, such that a standard photolithography process can be used to mass-produce the devices in parallel. Various etching processes will be explored to reduce optical scattering from the sidewalls of the ZnO WGM cavities. Coupling of ring devices has been shown to produce single mode lasing as is shown in [6]–[10]. Single mode lasing is desirable in many sensing applications however the devices need to be very close together which can make fabrication difficult and expensive. The use of optofluidcs can allow two devices to be coupled together that have a greater distance between them. This cuts back on fabrication difficulty and costs.

The fabrication and integration of these sensing and lasing capabilities is of interest to the Air Force as they meet several of the objectives of the Air Force Office of Scientific Research (AFOSR). Two examples of these objectives are "Laser and Optical Physics" and "Optoelectronics and Photonics." AFOSR's objective in "Laser and Optical

Physics" is "to advance the science of laser devices, laser materials, laser matter interaction, nonlinear optical phenomena and devices, and unique applications of these to solving scientific and technological problems of interest to the Air Force" [11]. This study meets this objective by focusing the use of optofluidic coupling and the use of ZnO as the WGM resonator material, neither of which have been widely explored. This study also helps meet the objective of AFOSR in looking for optoelectronic and photonic devices that are low power and weight and small sized [11]. Additional AFOSR objectives that this study helps include: Dynamic Materials and Interactions, GHz-THz Electronics and Materials, Low-Density Materials, Materials with Extreme Properties, Atomic and Molecular Physics, Electromagnetics, Quantum Information Sciences, Remote Sensing, Ultrashort Pulse Laser-Matter Interactions, Biophysics, Molecular Dynamics and Theoretical Chemistry, and Organic Materials Chemistry [11]–[13]. Further discussion of how WGM resonators have already contributed to some of these objectives will take place in Chapter II.

1.2 Assumptions/Limitations

Some of the main limitations of this study were choosing the geometries of the WGM resonators and the material to use. Chapter II will consider some of the other geometries as well as other material that has been used to make WGM resonators. Ring and disk geometries were chosen for this work because of the ease of fabrication and their repeatability which is necessary for mass production. ZnO was chosen as the material primarily for its high photostability.

The other main limitations for this work were the timeline and lab availability. Much of the fabrication work had to be done at AFIT, however some needed to be coordinated with the Air Force Research Laboratory (AFRL). The AFIT clean room was closed for several months due to the COVID-19 pandemic. Once the lab reopened there were several equipment failures that hindered devices characterization. These included the scanning electron microscope (SEM) and profilometer. Repairs for this equipment took long than normal due to COVID-19 restrictions and they are both still down as of the writing of this thesis. The testing of the devices also had to be done at AFRL. However, due to COVID-19 protocols, lab access was halted here also for several months. Then when the labs reopened, access was only granted one day, and later 2 days, per week. This made consistent testing difficult and caused delays in the process. Another limitation was the power of the lasers available at AFRL. In order to get the necessary intensity needed to excite the fabricated WGM resonators, the beams needed to be focused down between 1 – 5 μm. This is much smaller than the diameter of even the smallest device tested (100 μm). Another more powerful laser became available from the Department of Engineering Physics at AFIT (AFIT/ENP) late in the study but when it was moved and set up in the labs at AFRL, the laser could not be turned on because of high humidity on the laser crystal.

General assumptions were made with regards to the environment of the lab in which the tests were conducted. This included assuming relative humidity, ambient temperature, and atmospheric pressure.

1.3 Potential Contributions

Potential contributions from this work to the defense-focused research of AFIT include:

- Successful fabrication of ZnO ring and disk WGM resonators.
- Coupling of two WGM micro-resonators using optofludics.
- Single mode lasing from coupled WGM resonators.
- Demonstrated ease of fabrication and repeatability of the fabrication process for mass production.

1.4 Thesis Overview

This thesis is divided into five chapters. Chapter II will be a literary view of past WGM resonator devices as well as other ZnO lasers, including WGM cavities, Fabry-Pérot (FP) cavities, and nanotubes. The basic physics discussion will also be included here. Chapter III will give an overview of the methodology used in the design, fabrication, and testing of the devices. Chapter IV will give a thorough discussions on the results of the testing. Chapter V will offer the conclusion and the next steps for future research.

II. Literature Review

2.1 Chapter Overview

This chapter will discuss the basics physics concepts used in this work to understand the WGM resonator. This will include looking at the WGM resonator as a wave guide and how to couple two such waveguides together. Next, past WMG devices and their applications will be reviewed. Finally, this chapter will review past laser applications that use ZnO.

2.2 Optics and Physics of the Whispering Gallery Mode

A whispering gallery mode (WGM) is a useful optical resonator that uses total internal reflection to capture a wave of light. It can be made in many different geometries including microrings, microspheres, mirogoblets, microdisks, microbubbles, and microtoroids [14]. For this research, only the microring and microdisk geometries are being considered. The calculations for complete understanding of how a WGM resonator works can be quite complex and intensive and has been shown in other works such as [14]–[17]. However, reasonable approximations can be used to understand the workings of the WGM resonator. This will include geometrical optics and waveguide theory. In order for the wave of light to experience total internal reflection within the WGM resonator the angle of incident must be greater than the critical angle [15]. This phenomenon is shown in Figure 1.

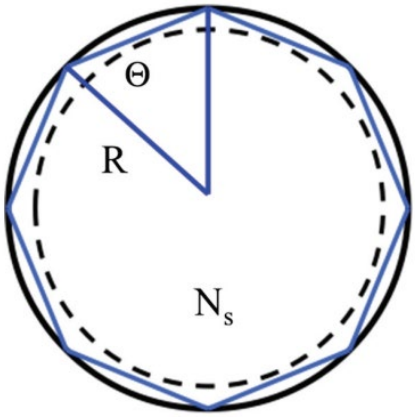

Figure 1. Total internal reflection of light in a WGM. Here Θ is the angle of incidence, R is the radius of the circle, and N_s is the refractive index [15].

This critical angle can be found using equation 1.

$$\theta_c = \arcsin(\frac{1}{N}) \tag{1}$$

Here, N, is the index of refraction of the WGM resonator. The wave must constructively interfere with itself as it travels along the WGM, meaning that the optical path length must correspond to an integer number of wavelengths and to the circumference of the WGM as is shown in equation 2

$$2\pi NR = l\lambda \tag{2}$$

where l is an integer. This constructive interference allows for the WGM to act as the optical cavity of a laser and allows for multimode lasing.

One of the easiest ways to get light reflecting within at WGM is to couple light in from another wave guide. A simple illustration of this is shown in Figure 2 [18].

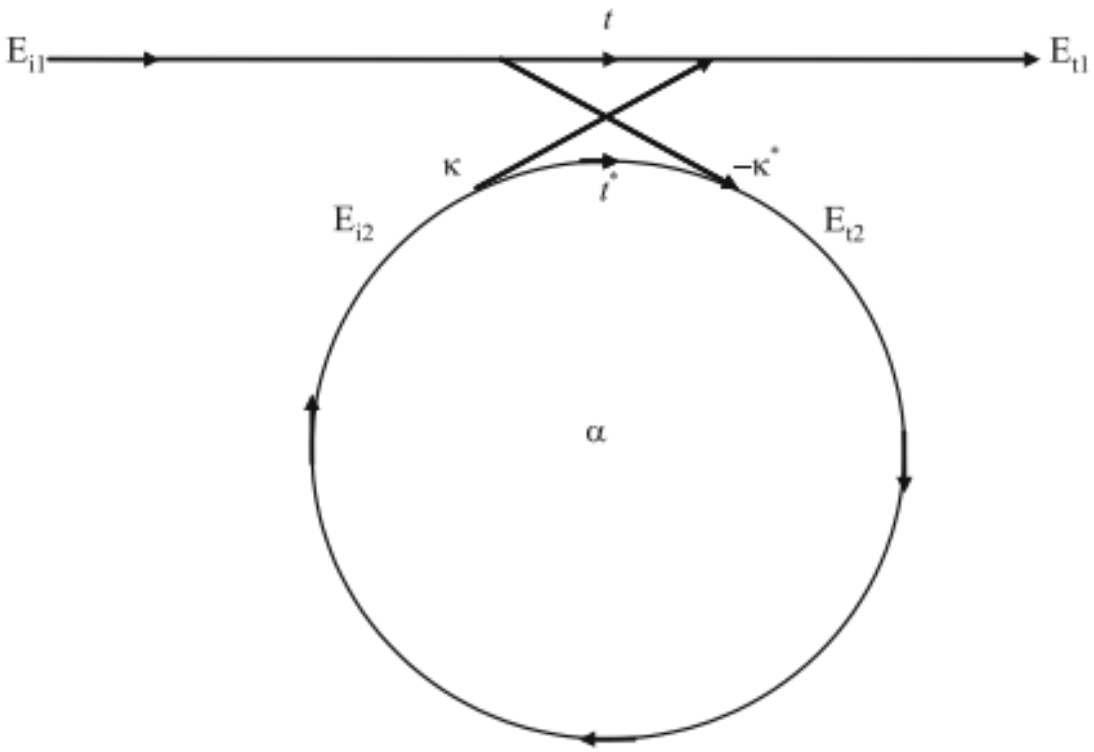

Figure 2. A simple diagram of a single ring and single waveguide coupling a unidirectional mode. The arrows are the direction of propagation. Reprinted by permission from Springer Nature: Copyright © 2020.

In this diagram, E is the amplitude of the electric field as it propagates through the waveguide and ring resonator, α is the loss coefficient, t is the transmission constant, and κ and is the coupling constant. The value that is of the most interest in this study is that of κ. The coupling constant is used to find the distance in which the two waveguides can be separated while still being able to couple. The κ value can be estimated by equation 3 [9].

$$\kappa = \left[\frac{2\pi R}{\gamma} e^{\left(-\frac{(\Delta\beta)^2 R}{r}\right)}\right] \frac{k^4}{4\beta_{RR}\beta_{WG}} (n_{WG}^2 - n_S^2)(n_{RR}^2 - n_S^2) \\ * \int_{WG} e_{WG} e_{RR} dx \int_{RR} e_{WG} e_{RR} dx \quad (3)$$

The definitions of the constants used in the above equation are shown in Table 1.

Table 1: Defined Constants for Equation 3.

R	Ring Radius
γ	Decay Constant of Ring
B	Propagation Constant
k	Wave Number
n	Refractive Index
e	Evanescent Electric Field Distribution

The subscripts RR, WG, and S refer to the ring resonator, waveguide, and substrate, respectively. The coupling constant can also be estimated through simulation as has been shown in [9]. This was accomplished by using the finite element analysis (FEA) of the ring resonator and the waveguide and plotting their respective evanescent fields. The two fields were then plotted along the same x axis at different coupling distances and the integral of their overlap is used in the equation above to estimate the κ value. This is the method that will be employed for this work and will be shown in Chapter 3.

One interesting phenomenon of coupling waveguides is that single mode lasing is possible by coupling two WGM resonators of differing diameters together through what is called the Vernier Effect [6]–[8], [10], [19], [20]. When two resonators are coupled, the resonant modes can affect each other so that so one mode is greatly improved, and the other modes are suppressed [6]. The resonant wavelength, λ_0, of one of the ring resonators can be found by simply rewriting equation 2 below [8].

$$M\lambda_0 = \pi D_2 n_{eff} \tag{4}$$

Here M is an integer, D_2 is the diameter of the ring, and n_{eff} is the effective refractive index. Once the resonance of the first ring is found, the diameter needed for the second ring can be found using the same λ_0 and n_{eff} from equation 4 in equation 5 [8].

$$N\lambda_0 = \pi D_1 n_{eff} \tag{5}$$

Equation 6, also known as the Vernier equation, can then be used to find the spectral separation of the two rings [8], [20].

$$\Delta\lambda = \frac{\lambda^2}{\pi n_{eff}(D_1 - D_2)} \tag{6}$$

Figure 3 below is a simple diagram showing how the Vernier effect works with coupled WGM resonators. In this case the WGM resonators are staked on one another, though the same affect can happen when they are coupled next to each other.

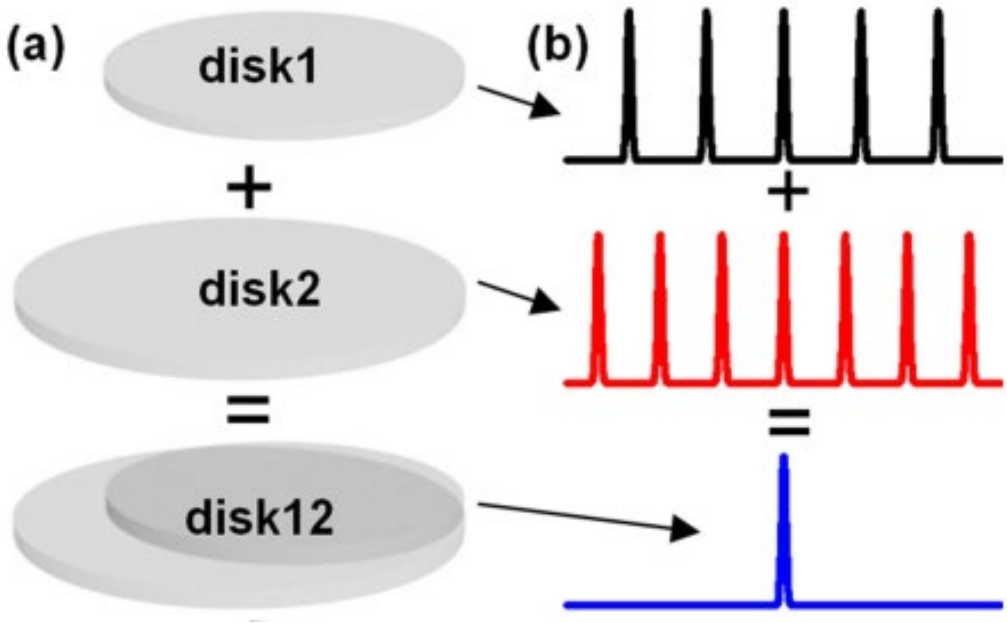

Figure 3. (a) A simple diagram of how two WGM disks can be coupled together. (b) and illustration of how the Vernier effect works to produce a single mode laser as most of the modes from the two disks destructively interfere while one mode constructively interferes and is emitted by the devices [7]. Copyright © 2015 IEEE.

One of the great advantages of WGM resonators is their very high quality factor (Q-factor). The Q-factor can be defined using equation 7 [16]:

$$Q = \frac{\omega_0}{\Delta\omega_{FWHM}} \tag{7}$$

Where ω_o is the resonant angular frequency and $\Delta\omega_{FWHM}$ is the full width at half maximum of the resonant angular frequency. The Q-factor is important because it gives a way to measure the time it takes for the energy to dissipate from a resonator in terms of its full field oscillations. This means that a higher Q-factor corresponds to a slower energy dissipation and a more efficient resonator [16]. In addition to the definition above, the intrinsic Q-factor can be found through the contribution of many losses [15]:

$$\frac{1}{Q_{ins}} = \frac{1}{Q_{rad}} + \frac{1}{Q_{scat}} + \frac{1}{Q_{mat}} + \frac{1}{Q_{cont}} \tag{8}$$

Where Q_{rad} is the loss due to the curvature, Q_{scat} is the loss due to scattering along the surface, Q_{mat} is the loss due to material absorption characteristics, and Q_{cont} is the loss due to surface contaminates. The main factor for loss in a WGM resonator has been shown to be due to absorption loss associated with the material chosen [21]. The high Q-factors for WGM resonators are inherent in the fact that they are low loss devices. Q-factors for WGM resonators have been recorded at values greater than 10^{10} [14]–[16]. Each of the factors in this section have made WGM resonators highly desirable for many applications.

2.3 Past Optofludic Devices

Optofluidic devices have become a source of increased excitement in the research community. These are devices in which photonic and microfluidic designs are integrated to enhance the performance and function of the device [22]. Areas that have seen particular interest are those of refractive index (RI) based detection sensors, fluorescence-

based sensors, surface-enhanced Raman spectroscopy, and optical trapping and manipulation [22]. An example of several RI detection sensors is shown in Figure 4.

Optofluidics has been applied in many different ways and is particularly useful in biological and chemical detection and analysis. It allows for the use of extremely small volumes and integrates the sample preparation and delivery with the analytics used for detection [22]. In addition to biosensing, optofluidic lasers are also an area of great interest. Many groups have shown the optofluidic lasers in use as a distributed feedback (DFB) laser on a chip [23]–[27]. While these devices show low pump threshold, tunable wavelengths and single mode emission, their manufacturing is not straight forward and is expensive [28].

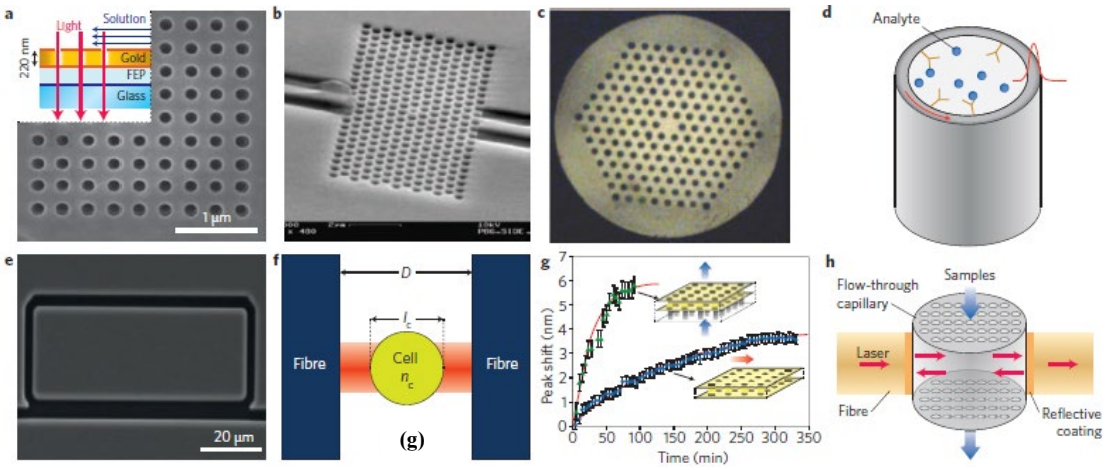

Figure 4. Several optofluidic devices that are used in RI detection [22]. (a) Metallic nanohole-array-based plasmonic sensor. (b) Dielectric planar photonic crystal sensor. (c) PCF-based sensor. (d) Capillary-based OFRR sensor. (e) ARROW-based OFRR. (f) Fabry-Pérot interferometric sensor for cell detection. (g) Flow-through and flow-over plasmonic sensors together with each system's sensing response. (h) Fabry-Pérot sensor with flow-through micro- and nanofluidic channels. Reprinted by permission from Springer Nature: Copyright © 2011.

Other proven devices include Fabry-Pérot cavities that use fiber-based mirrors and are integrated with microfluidic dye have shown single mode emission and digital programmability [29]–[32]. However, the process of coating the cavity is laborious and difficult to implement into a monolithically integrated system. It also has a multistep assembly which negatively affects its compactness and robustness [28]. Another optofluidic laser device that has been shown is based on a two-dimensional photonic crystal that was patterned by laser interference lithography [33], [34]. This has enhanced spontaneous emission, a low lasing threshold, and avoids using e-beam lithography. However, it does take highly customized and difficult optical alignments to pattern each device, which is very difficult to use in manufacturing and integrating into practical systems. The work of this thesis will overcome each of these difficulties. The process shown will use standard, and easily repeatable lithography steps that will allow for inexpensive manufacturing on a large scale. The devices will be patterned on a chip for easy integration into other systems and can allow for different wavelength emission.

2.4 Past Whispering Gallery Mode Devices

WGM resonators have been extensively studied for use in many ways. This section will look at just a few studies of optofluidic integration and single mode emission through the Vernier effect. The integration of optofluidics with WGM resonators has led to increased sensing application, especially in biological and chemical sensing [35]. Optofluidic WGM resonators can investigate a gain medium that is introduced as a fluid. This allows for the necessary sensitivity needed in biosensing to detect DNA and protein [35]. Additionally, the narrow linewidth of optofluidic WGM lasers could enable the

detection in frequency shifts induced by single molecules [35]. Examples of WGM resonators using optofluidics in biosensing are shown in Figure 5.

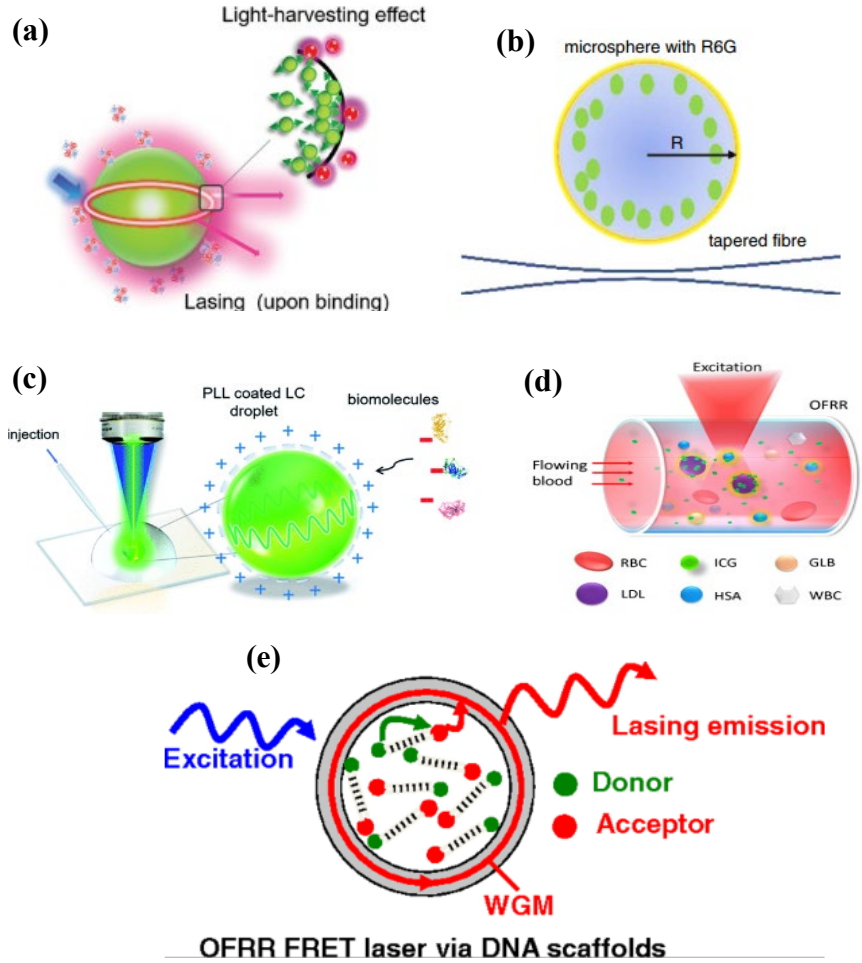

Figure 5. (a) A lasing encoded microsensor driven by interfacial cavity energy transfer used for molecular barcoding [36] Copyright © 2020, John Wiley and Sons. (b) A WGM laser cavity with a rhodamine 6G gain medium used to detect a change in refractive index [37] Copyright © 2006, IEEE. (c) Bioelectrostatic sensitive droplet lasers using liquid crystals used for ultrasensitive biosensing and monitoring of molecular interactions [38] Published by The Royal Society of Chemistry. (d) Optofluidic ring resonator (OFRR) that uses fluorophore laser emission for detecting albumins, globulins, and lipoproteins in blood [39]. (e) Another OFRR used for intracavity biological and chemical sensing, bio-controlled photonic devices, and biophysics [40].

Each of these devices show the great benefit that can come from integrating optofluidics and WGM resonators. This work will differ from the works above though in that the optofluidics will be used to help couple the WGM resonators and will not be used as the gain medium.

Along with successful integration with optofluidics, WGM resonators have also successfully shown single mode emission. Chandrahalim et al. were able to successfully show WGM multimode and single mode emission with on-chip solid-state dye-doped polymer ring resonators [10]. In their work they were able to fabricate single and coupled WGM ring devices into a fused silica substrate through reactive ion etching (RIE). After fabrication, several dye-doped polymers were spin-coated on to act as the medium for the pump laser. The devices were then excited by a pump laser at various wavelengths ranging from 480-570 nm depending on the doped polymer used. Successful multimode emission was shown from the single ring WGM resonator, as well as successful single mode emission from the coupled WGM resonators. Results from their research are shown in Figure 6 and Figure 7.

Their impressive work differs in a few ways though from the focus of this thesis. The doped polymer needed for laser emission adds another fabrication step where this thesis just has the single etching step. This work will also focus on using simple cleanroom wet etching techniques rather than the RIE technique used in this work. Further dye-doped polymer WGM lasers have been shown in [41]–[47].

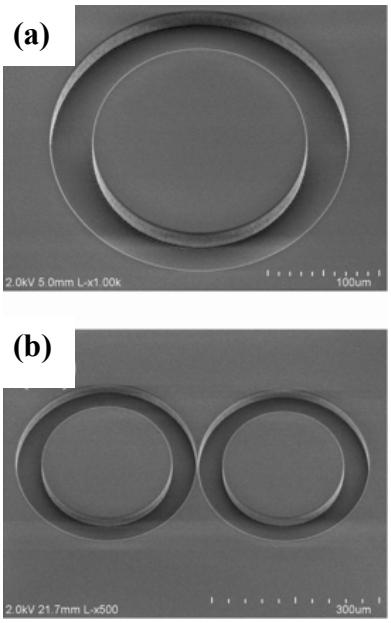

Figure 6. Scanning electron microscope images of the fabricated ring resonators: (a) Single ring resonator with inner and outer radii and depth of 110, 150, and 12 μm, respectively. (b) Coupled ring resonators with an outer radius of 150 μm and 145 μm, respectively. Both ring resonators are 40 μm wide and 12 μm deep. The coupling distance between the two rings is approximately 1 μm [10].

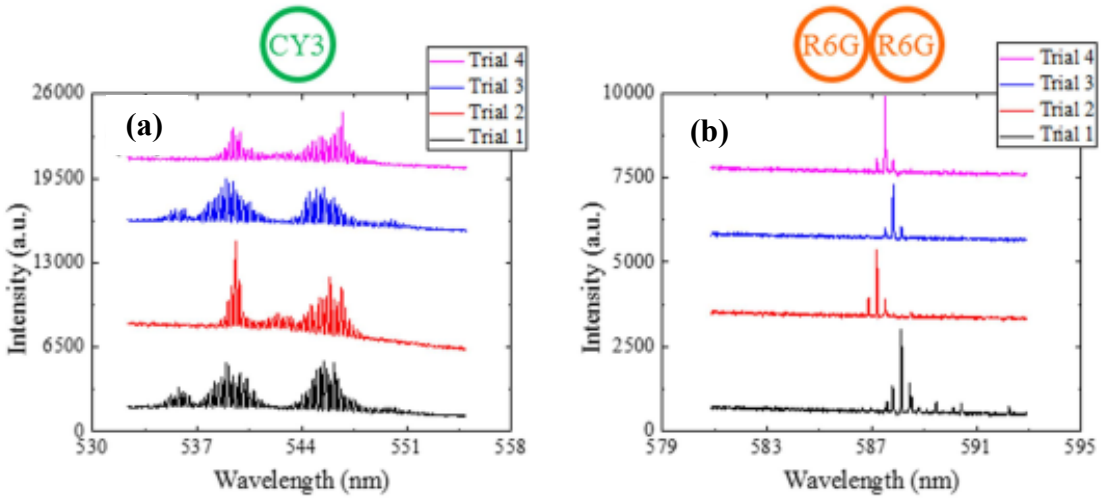

Figure 7. (a) Emission spectra of a CY3-doped SU-8 single ring resonator laser with a 16 μJ/mm^2 pump intensity. A 1200 g/mm grating was used to capture the entire detectable laser emissions. (b) Emission spectra of an R6G-doped SU-8 coupled-ring resonator laser with a 6μJ/mm^2 pump intensity. A 2400 g/mm grating was used to achieve high spectral resolution. All spectra are vertically shifted for clarity [10].

Another example of coupled WGM devices used in single mode emission is shown in [20]. Here Lee et al. were able to make two ring devices couple together for single mode emission, and then couple the rings to a waveguide as is shown in Figure 8.

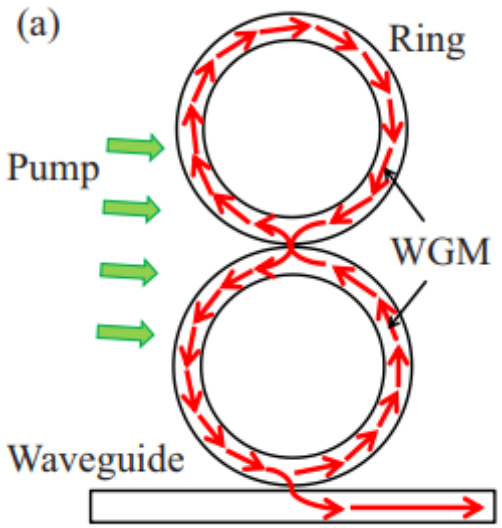

Figure 8. A schematic of coupled rings and waveguide. The arrows show the light propagation direction [20]. Reprinted fromW. Lee, H. Li, J. D. Suter, K. Reddy, Y. Sun, and X. Fan, "Tunable single mode lasing from an on-chip optofluidic ring resonator laser," *Appl. Phys. Lett.*, vol. 98, no. 6, pp. 2011–2014, 2011, doi: 10.1063/1.3554362. with the permission of AIP Publishing.

This device was produced in polydimethylsiloxane (PDMS) by means of a mold and then liquid was added to the device to create an optofluidic ring resonator (OFRR). The mold was etched into a silicon wafer through RIE. The wafer was then coated with PDSM which was cured and removed to create the device above. Dye dissolved in tetraethylene glycol TEG is then added to the rings and just TEG is added to the waveguide to serve as the mediums for the light propagation. Examples of the OFRR is shown in Figure 9.

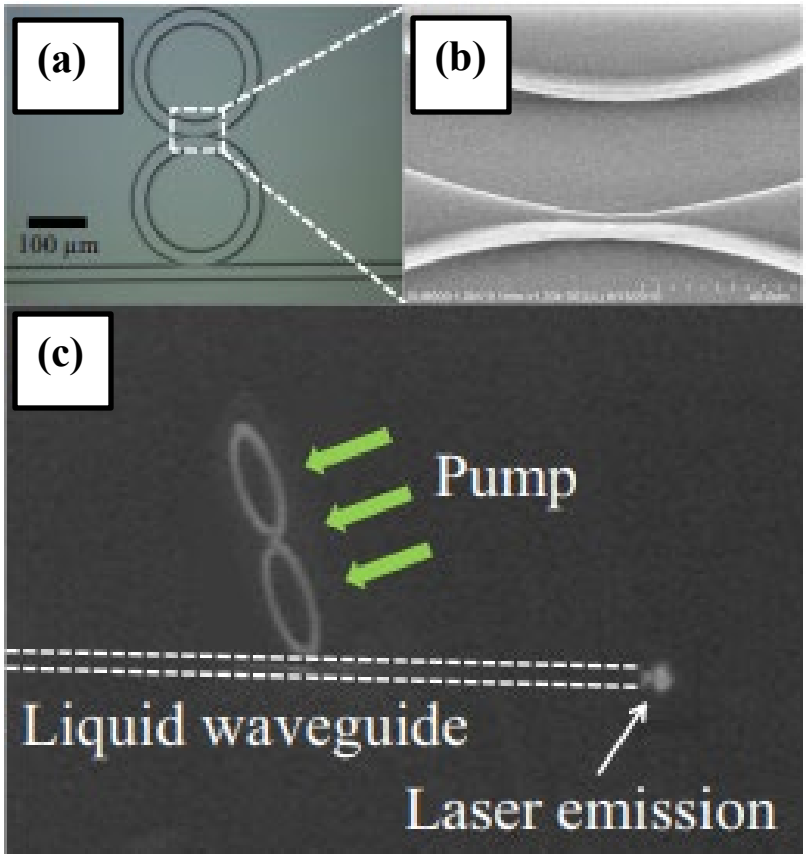

Figure 9. (a) Image of the coupled OFRR formed on the PDMS substrate. The diameters of the upper and lower ring are 290µm and 300 µm, respectively. The gaps between the lower ring and the waveguide and between the two rings are 2 µm and 1 µm, respectively. (b) Scanning electron microscopic image of the 1 µm gap between the two rings. (c) Photograph of the coupled OFRR during laser operation. The laser emission is coupled into the liquid waveguide and collected at its distal end. Dashed lines show the waveguide position [20]. Reprinted fromW. Lee, H. Li, J. D. Suter, K. Reddy, Y. Sun, and X. Fan, "Tunable single mode lasing from an on-chip optofluidic ring resonator laser," *Appl. Phys. Lett.*, vol. 98, no. 6, pp. 2011–2014, 2011, doi: 10.1063/1.3554362. with the permission of AIP Publishing.

The rings are then pumped at 532 nm and single mode emission is achieved. The results are shown in Figure 10.

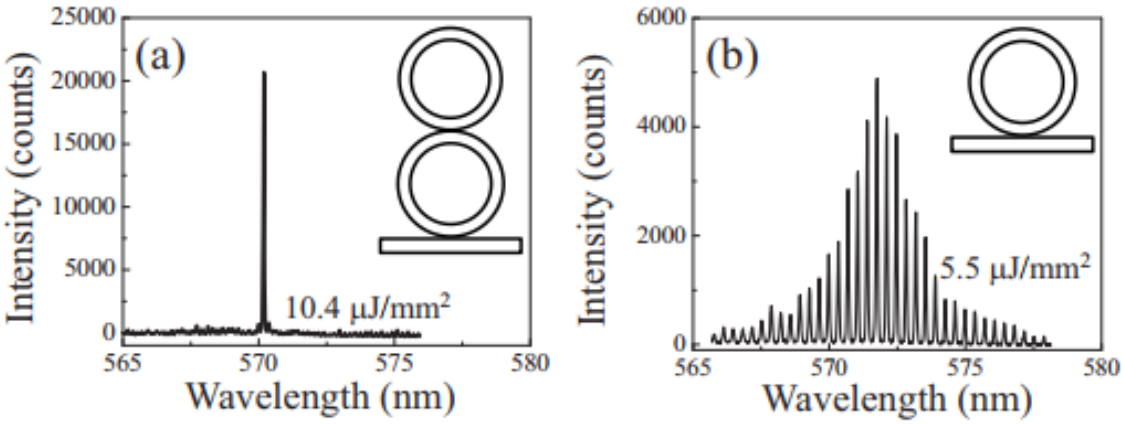

Figure 10. (a) Lasing spectrum from a coupled OFRR 190 μm and 200 μm in diameter, respectively. The gaps between the lower ring and the waveguide and between the two rings are 2 μm and 1 μm, respectively. (b) Lasing spectrum from a single OFRR 200 μm in diameter. Gain medium is 2 mM R6G in TEG. Reprinted fromW. Lee, H. Li, J. D. Suter, K. Reddy, Y. Sun, and X. Fan, "Tunable single mode lasing from an on-chip optofluidic ring resonator laser," *Appl. Phys. Lett.*, vol. 98, no. 6, pp. 2011–2014, 2011, doi: 10.1063/1.3554362. with the permission of AIP Publishing.

While this is impressive, the processes of making the PDSM mold is cumbersome. Also, PSDM is a polymer that cannot withstand high pressure or strong solvents, which limits its application. The single step fabrication that this thesis will study will make the realization of single mode emission quicker and easier, and the devices will be more robust. Other examples of OFFRs are found in [48]–[54]. Other examples of PDSM based OFFRs are found in [40], [55].

An example of an WGM resonator using optofludics is shown in [56]. This work shows a 3-D optofluidic WGM resonator fabricated using a femtosecond laser machining process. The resonator can then accommodate any organic, inorganic, and biological gain media. An example of such a device is shown in Figure 11 [56].

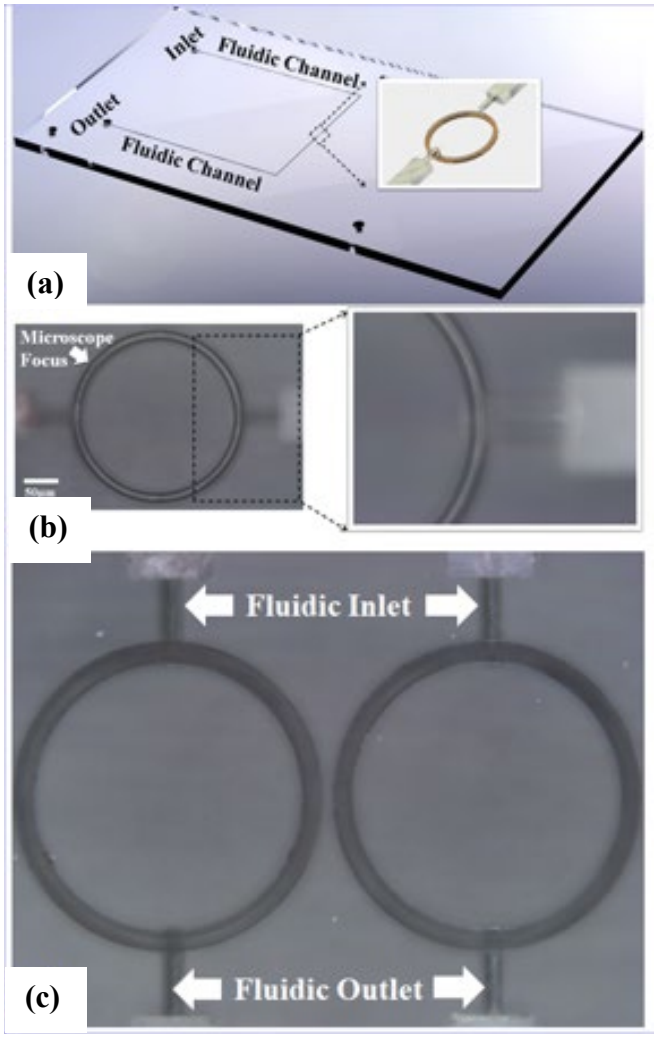

Figure 11. (a) Schematic of 3-D optofludic WGM ring cavity fabricated by femtosecond laser pulses; (b) Microscope image of the ring cavity with the focus on the ring section; (c) A coupled optofluidic WGM ring resonators.

Patterning these devices consisted of exposing a fused-silica substrate to femtosecond laser pulses from a Ti: sapphire laser operating at 800 nm. The pulse width was approximately 100 fs and the repetition rate was set at 250 kHz. A long-working distance microscope objective was used to focus the beam into the sample. The laser writing speed depends on the local geometry of the structure, but can range from 100

μm/s to 5 mm/s. The laser pulse energy was adjusted so that there was no material ablation associated with the writing step. Both transverse and longitudinal polarizations of the laser beam were used for the exposure. After the exposure, the substrate was immersed into a low-concentration aqueous solution of hydrofluoric acid. These optofluidic WGM resonators consist of 3-D microfluidic channels that can have fluidic gain media dynamically flow in real time.

This work is commendable, but the fabrication of these devices can be difficult. The devices shown in this thesis will be made using standard photolithography techniques. The ZnO WGM resonators will also be solid material that will use reconfigurable high refractive index liquids to facilitate the evanescent coupling between the devices.

In addition to the two examples above, many other studies had looked at the use of WGM resonators. These include ultra-sensitive sensors, even quantum sensing [57]–[61], many lasing applications [62]–[65], and even in detecting cancer [14]. Like the examples discussed above, these applications are impressive, though they are often hard to replicate or very expensive to implement. This work will show fabrication and development techniques that will help drive down the cost and increase the ability to reproduce WGM devices. This will be accomplished by using standard lithography and etching techniques that allow for simple WGM ring and disk geometries. The next step will be to couple two of these WGM resonators (either two rings or two disks) together to create a single mode laser. Typically coupling two WGM resonators requires that they be within nanometers of each other, which can be difficult and expensive to do. However, dynamically reconfigurable high refractive index liquids can be used to facilitate the

evanescent coupling between WGM ring cavities, such that the coupling gap between rings can be relaxed and a standard photolithography process can be used to fabricate many devices in parallel. This offers the solution to many of the issues of cost and reproducibility of WGM devices.

2.5 Past ZnO Laser Applications

ZnO, is one semiconductor material of particular interest in lasing applications because of its high photostability. It has been used to create Fabry-Pérot (FP) cavity lasers [66]–[68], random lasers [69], [70], and even WGM lasers on microrods [71]–[74]. ZnO lends itself well to small device fabrication. The FP lasers range from the 10s of microns to the 100s of nanometers. This was first shown by Huang et al. who were able to show a lasing peak of 385 nm when pumped by the fourth harmonic of a neodymium-doped yttrium-aluminum-garnet laser (Nd: YAG; 266 nm, 3 ns pulse width) [75]. In this work, <0001> oriented ZnO nanowires were grown by vapor transport and condensation process with diameters varying from 20 to 150 nm and lengths of up to 10 mm. When pumped with an intensity of about 40 kW/cm2, a lasing peak with an emission linewidth of around 300 pm was observed. The results of their work are shown in Figure 12.

The sizes of these devices are desirable for use with other systems without adding much bulk, but it can be very challenging to integrate optical waveguides on the same substrate that are needed for intra- and inter- chip optical connectivity. It is also difficult to duplicate these devices as they are grown randomly on the substrate. They also have high mirror losses because of a low reflectivity of 0.2 at the air/ZnO interface and short cavity lengths.

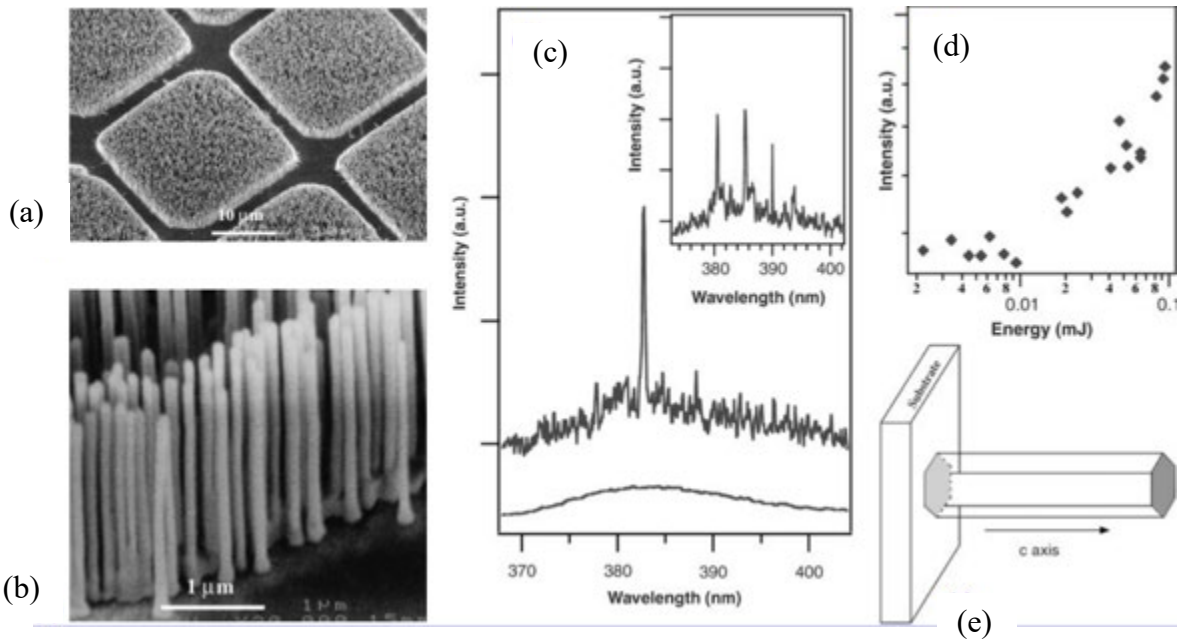

Figure 12. (a) and (b) SEM images of ZnO nanowire arrays grown on sapphire substrates, (c) Emission spectra from nanowire arrays below and above the lasing threshold. The pump power for these spectra are 20, 100, and 150 kW/cm2, respectively; (d) Integrated emission intensity from nanowires as a function of optical pumping energy intensity; (e) Schematic illustration of a nanowire as a resonance cavity with two naturally faceted hexagonal end faces acting as reflecting mirrors [75]. From M. H. Huang *et al.*, "Room-Temperature Ultraviolet Nanowire Nanolasers," *Science (80-.).*, vol. 292, no. 5523, pp. 1897–1899, 2001, doi: 10.1126/science.1060367. Reprinted with permission from AAAS.

The random lasers are relatively simple to fabricate as a polycrystalline ZnO which is desirable. An example of this is shown in [76]. In this study, mirrorless ZnO thin-film waveguides are deposited on a (100) silicon substrate. The laser cavities, due to closed-loop optical scattering from the lateral facets of the irregular ZnO grains, are generated through the post-growth annealing of high-crystal-quality ZnO thin films. The lasing wavelength and linewidth of the ZnO random lasers under 355 nm optical

excitation are around 390 nm and less than 0.4 nm, respectively. Results from this work are shown in Figure 13.

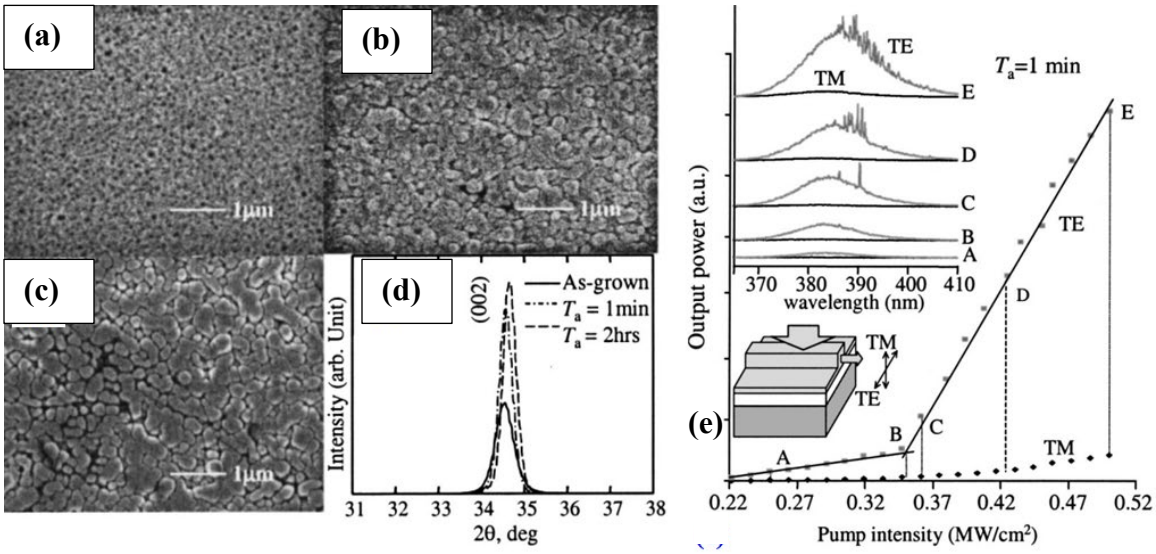

Figure 13. SEM images of ZnO thin films: (a) as-grown, (b) annealing time of 1 minute, and (c) annealing time of 2 hours. (d) The corresponding X-ray diffraction patterns of the ZnO film. (e) Light–light curves and the emission spectra of the sample after post-growth annealing for annealing time of 1 minute [76].

Random lasers can be relatively simple to reproduce on the substrates; however, the nature of random lasers does not yield repeatable results that are desirable in many sensing applications. The WGM lasers are also on the 10s of micron scale when fabricated as a crystal structure. This is due to its highly c-axis orientated hexagonal crystal structure. This hexagonal shape can naturally be used as a WGM cavity. This can has been shown by Dai et al. [77]. An individual ZnO WGM microrod is isolated on a quartz wafer. The excitation laser at 355 nm wavelength was focused onto the ZnO microrod with an incident angle of around 60°, and the emission signal at different angles was collected by moving

the collect facet of a fiber along a circular path. The results of this study are presented in Figure 14.

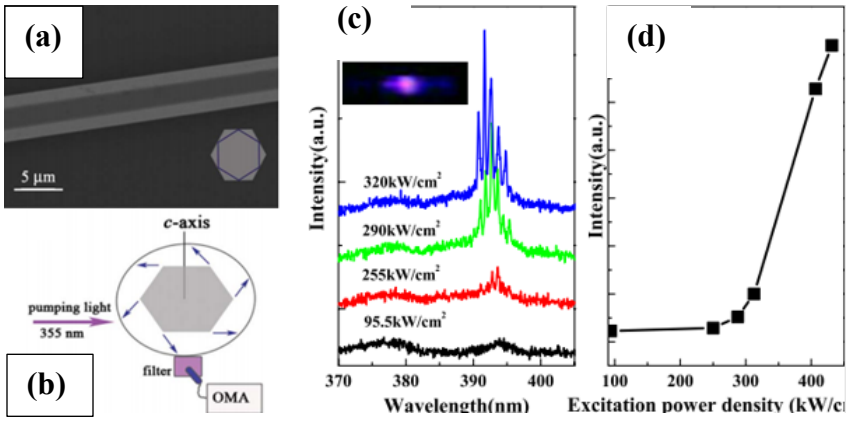

Figure 14. (a) SEM image of a ZnO hexagonal microrod with a schematic WGM cavity and the light propagation path. (b) The schematic diagram for the lasing detection around the hexagonal ZnO microcavity. (c) Emission spectra of the ZnO microrod excited by a Nd:YAG laser with different excitation intensity. The inset is the far-field image of the lasing ZnO microrod taken by a digital camera. (d) The relationship between output lasing intensity and excitation power density [77].

While this microstructure occurs naturally, it can be difficult to control the growth of the micro rods and it can be difficult to integrate them into sensing applications. Their small radius also contributes to greater losses.

2.6 Summary

WGM resonators have been extensively studied in many works. Their low losses and ability to obtain high Q- factors even when developed on chip has made them desirable for many applications. Their ability to produce single mode emission by coupling two WGM resonators together also makes them ideal for sensor applications.

This work will focus on developing simple and repeatable fabrication of ring and disk WGM geometries of ZnO. It will use simple lithography steps and inexpensive etching techniques to produce highly repeatable structures that can be integrated easily into other systems. It can then be used to produce high quality lasing by coupling two structures together by use of optofluidics through the Vernier effect. The details of these claims will be explored further in chapter III.

III. Methodology

3.1 Chapter Overview

The purpose of this chapter is to lay out the steps that were taken in the design, fabrication, and testing of the WGM devices used for this study. It was decided that ring and disk shapes would be used because of the ease of fabrication using standard clean room procedures. These devices also agree well with the theoretical WGM optical theory and their derivation is relatively straight forward. The design process began with a derivation of the size of waveguide needed for single mode emission. The size could then be increased to support multimode emission. Simulations were then done with COMSOL Multiphysics® Modeling Software. While working on the simulations, several different sized ring and disk devices were designed for testing the etching processes, and well as for some practical testing. The devices can easily be fabricated through either wet or dry etching. Wet etching was chosen as the preferred method since it is more cost effective, more convenient, and generally produces a smother etch surface that is desirable for optical applications. Ammonium Chloride (NH_4CL) was the etching chemical chosen since it is a relatively weak acid and has been shown to have low lateral etch[78], [79]. A 3 factor Design of Experiments was used to determine the ideal concentration and conditions for an optimal etch. Once an adequate etch process was defined, the devices were taken to a Photoluminescence (PL) lab at the Air Force Research Laboratory Sensors Directorate (AFRL/RY). Here an Ultraviolet laser was used to excite a device,

and the response was measured through a spectrometer. Each of the design, fabrication, and testing processes with be explored further in the following sections.

3.2 Design of ZnO WGM Optical Resonators

3.2.1 Derivation of ZnO WGM Resonators Dimensions

As was mentioned above, the design process began with the derivation of the size of waveguide that would be needed for single mode emission. It was decided that the area surrounding the devices would be etched away so that the actual devices were raised up above the substrate as is shown in Figure 15.

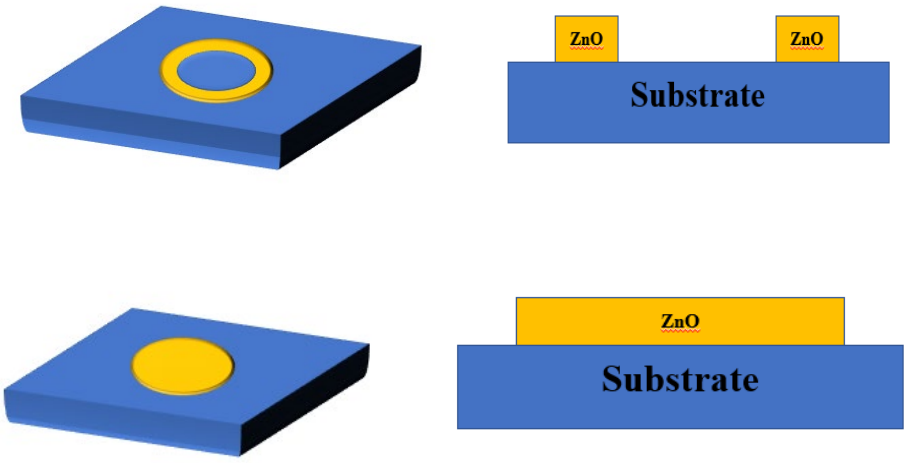

Figure 15. An example of a ring and disk WGM device that will be fabricated for this thesis and their cross sections.

For the purposes of this derivation, the ring device was treated as a straight wave guide with a square cross section. In his book, *Photonic Devices*, Liu talks about several

common wave guides and their derivations [80]. For the purposes of this derivation, the device is considered a planar wave guide as shown in Figure 16.

Figure 16. An example of a planar waveguide that is used for the derivation of the dimensions of the ZnO rings.

The modal properties of this waveguide can be characterized in terms of some dimensionless normalized wave guide parameters. One of these is the V number, or the normalized frequency [80], and it is defined by equation 9,

$$V = \left(\frac{2\pi}{\lambda}\right) d(n_1^2 - n_2^2)^{\frac{1}{2}} \tag{9}$$

where λ is the peak wavelength of the photoluminescent spectra of ZnO, d is the thickness of the planar wave guide, n_1 is the refractive index of ZnO and n_2 is the refractive index of air. By an approximation based on a well-known method of analyzing single mode fiber optics, $V = 15\pi$ can be assumed and inserted with the following values into (9): $\lambda = 371$ nm, $n_1 = 2.1$, and $n_2 = 1$. From this we get $d = 1.3$ µm. This value can then be applied to the thickness and width of the desired square waveguide. As long as

the dimensions of a waveguide are less than or equal to these values then light propagation should be possible.

In addition to looking at the dimensions above, it is important to confirm the reflectance of the WGM resonators that would be studied. For this, the power stored in a WGM resonator, P(λ), was found according to equation 10 and was graphed in MATLAB using a wavelength range from 323 nm to 327 nm [16].

$$P(\lambda) = P_0 \frac{(\Delta\lambda_{FWHM}/2)^2}{(\lambda - \lambda_0)^2 + (\Delta\lambda_{FWHM}/2)^2} \quad (10)$$

Here P_0 is the amplitude, λ_0 is the resonant wavelength, and $\Delta\lambda_{FWHM}$ is the full width at half maximum value of the resonance peak. Since it was known that the laser that we would be using for our experiments has a wavelength of 325 nm, this value was used as the resonant wavelength. $\Delta\lambda_{FWHM}$ was then found using equation 7, and theoretical Q-factors of 10^3, 10^4, and 10^5. The results are shown below in Figure 17.

Since the resonance has been confirmed for a laser with a wavelength of 325 nm, equation 2 can be used to find rings and disks of various radii that will support WGM propagation. For these calculations N = 2.1, λ = 325 nm, and *l* varies according to the table values. These radius values are shown in Table 2.

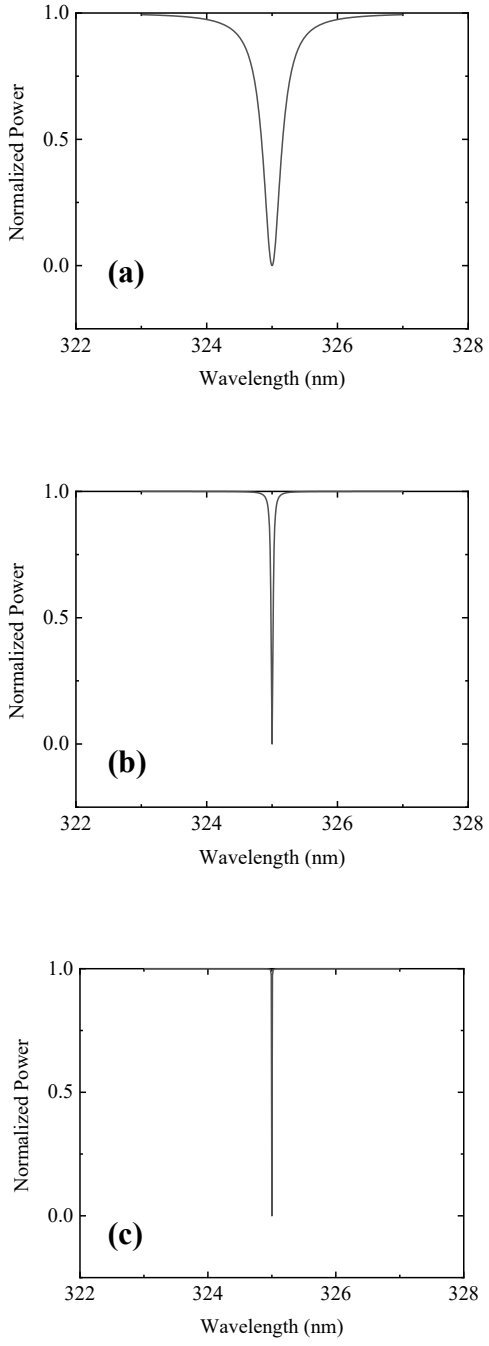

Figure 17. Normalized power of a WGM resonator confirming resonance at 325 nm. (a) Resonance when the WGM resonator has a Q-factor of 10^3. (b) Resonance when the WGM resonator has a Q-factor of 10^4. (c) Resonance when the WGM resonator has a Q-factor of 10^5. Each increase in the Q-Factor decreases the FWHM.

Table 2. Calculated Radii of Rings and Disks

***l* value**	**Radius in μm**
$2x10^3$	49
$3x10^3$	74
$4x10^3$	99
$5x10^3$	123
$6x10^3$	148
$7x10^3$	172
$8x10^3$	197
$9x10^3$	222
$10x10^3$	246

3.2.2 Simulation of ZnO Coupled Ring Resonators

Once the derivations for the various WMG dimensions were complete, simulation was done using the physics modeling software COMSOL. The purpose of this simulation was twofold. First was to show that propagation of light at a wavelength of 325 nm is possible with a ZnO ring. Second was to show that changing the index of refraction around the ZnO ring will widen the electric field distribution within the ring. This could be accomplished using different liquids surrounding the rings. This is very important for coupling as was discussed in section 2.2. The first simulation was done using the refractive index of bulk ZnO at 2.1. The refractive indices for the liquids in this simulation are hypothetical also. The other simulations were done using the refractive

indices of thin film ZnO. For thin films of less than 500 nm, 1.85 was used for the refractive index. For thin films between 500 nm and 1000 nm, 1.9 was used for the refractive index. The liquids used in the simulation are methylene iodide (CH_2I_2), n = 1.74, sulfur in methylene iodide (CH_2I_2), n = 1.79, and phenyldi-iodoarsine ($C_6H_5AsI_2$), n = 1.85. The parameters used in these simulations are shown in Table 3. Table 4, and Table 5. The results of these simulations are shown in Figure 18, Figure 19, and Figure 20.

Table 3. Parameters used in the COMSOL Simulation of a bulk ZnO Ring with hypothetical high refractive index liquids.

Wavelength	325 nm
Frequency	9.22×10^{14} Hz
Width	0.5 μm
Hight	810 nm
Refractive Index of Surrounding Material	1, 2, 2.05, 2.09
Refractive Index of ZnO Core	2.1
Refractive Index of Fused Silica Substrate	1.48

Table 4. Parameters used in the COMSOL Simulation of a thin film (less than 500 nm) ZnO Ring with various high refractive index liquids.

Wavelength	325 nm
Frequency	9.22×10^{14} Hz
Width	0.5 μm
Hight	400 nm
Refractive Index of Surrounding Material	1.74, 1.79
Refractive Index of ZnO Core	1.85
Refractive Index of Fused Silica Substrate	1.48

Table 5. Parameters used in the COMSOL Simulation of a thin film (between 500 nm and 1000 nm) ZnO Ring with various high refractive index liquids.

Wavelength	325 nm
Frequency	9.22×10^{14} Hz
Width	0.5 μm
Hight	800 nm
Refractive Index of Surrounding Material	1.74, 1.79, 1.85
Refractive Index of ZnO Core	1.9
Refractive Index of Fused Silica Substrate	1.48

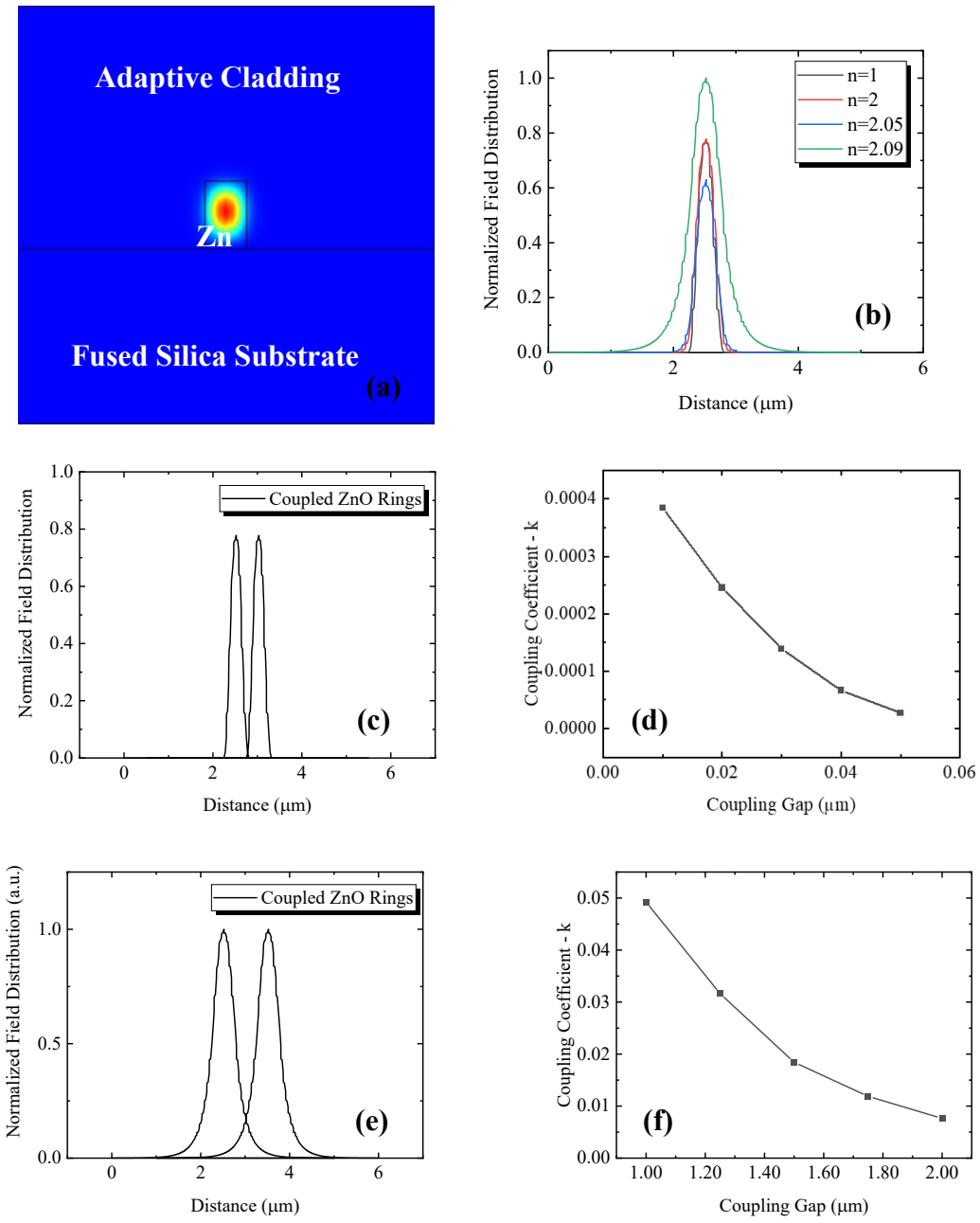

Figure 18. (a) COMSOL simulation showing light propagating within a ZnO ring where color represents the intensity of the transvers electrical (TE) mode. (b) Several field distribution curves as the refractive index surrounding the bulk ZnO ring is changed from n = 1 to n = 2.09. (c) Coupling shown by the overlap of two of the evanescent fields of two ZnO rings with a coupling distance of 10 nm and surrounded with a refractive index of 1. (d) A plot of the coupling coefficient (κ) between the two rings as a function of the coupling gap ranging from 10-50 nm. (e) Coupling of two ZnO rings when surrounded with a refractive index of 2.09. (f) A plot of κ between the two rings as a function of the coupling gap. The range is significantly larger, ranging from 1-2 μm, and as is the κ value.

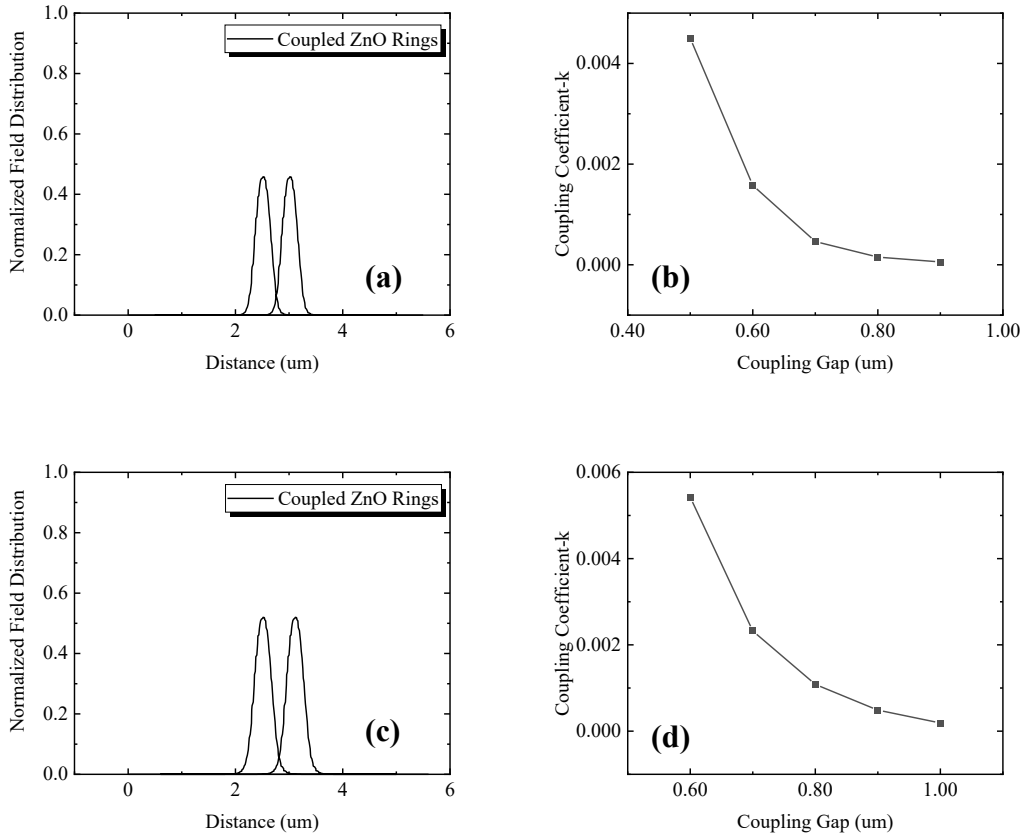

Figure 19. (a) Coupling of two thin film ZnO rings with a thickness of 400 nm (n=1.85) when surrounded with a refractive index of 1.74. (b) A plot of coupling coefficient (κ) between the two rings as a function of the coupling gap ranging from 500-900 nm. (c) Coupling of the same rings when surrounded with a refractive index of 1.79. (d) A plot of κ between the two rings as a function of the coupling gap ranging from 600-1000 nm.

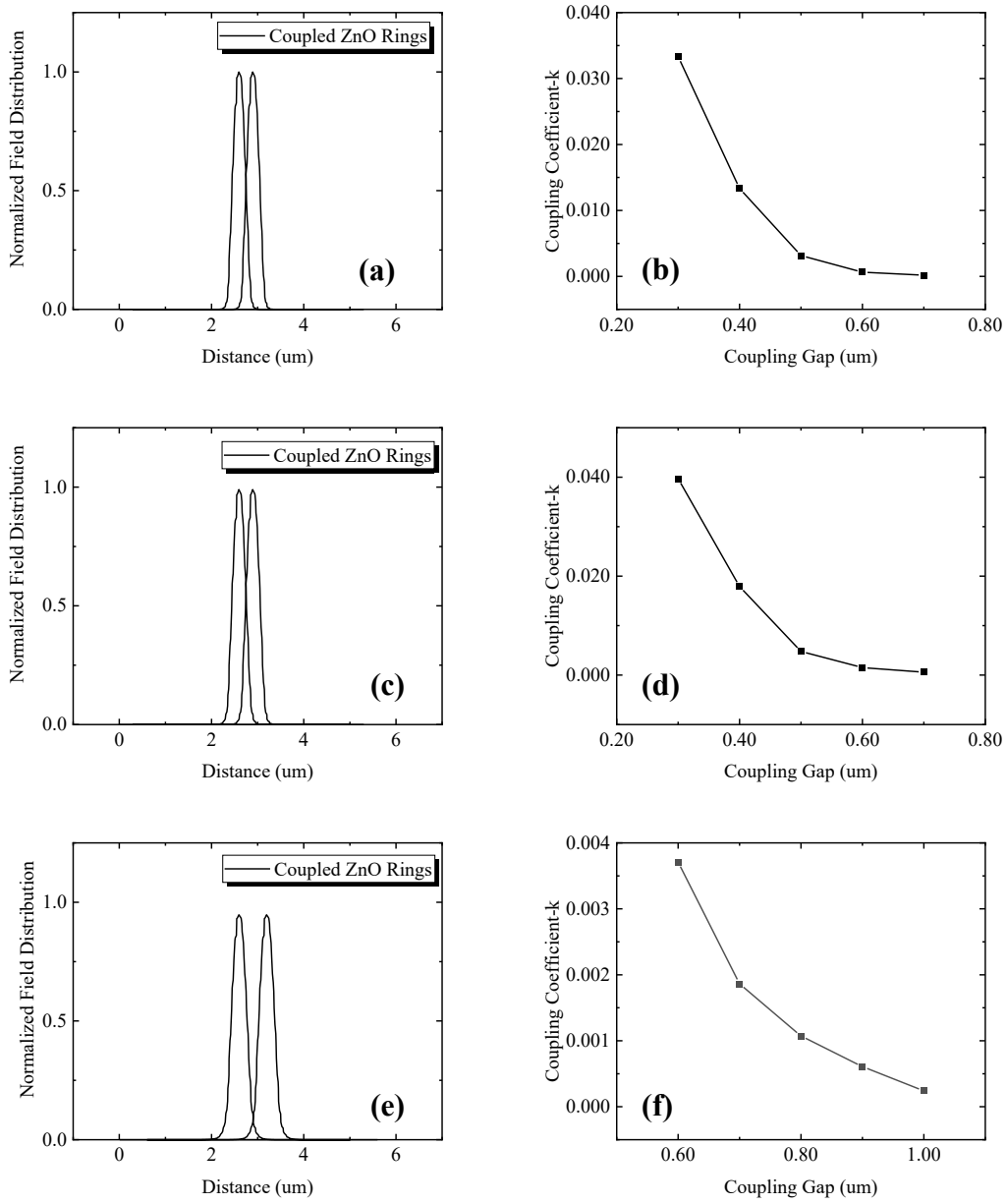

Figure 20. (a) Coupling of two thin film ZnO rings with a thickness of 800 nm (n=1.9) when surrounded with a refractive index of 1.74. (b) A plot of coupling coefficient (κ) between the two rings as a function of the coupling gap ranging from 300-700 nm. (c) Coupling of the same rings when surrounded with a refractive index of 1.79. (d) A plot of κ between the two rings as a function of the coupling gap ranging from 300-700 nm. (e) Coupling of the same rings when surrounded with a refractive index of 1.85. (f) A plot of κ between the two rings as a function of the coupling gap ranging from 600-1000 nm.

From Figure 18, this simulation shows that coupling can be accomplished at much greater distances with a high-refractive index liquid, which is very close to that of the ring, than in air. This is very promising for being able to fabricate these devices on a chip using standard lithography procedures. Figures 19 and 20 both show simulations of actual high refractive index liquids when compared to thin film ZnO. These simulations also show that the coupling distance is greatly increased over the simulation shown in air.

3.3 Fabrication of ZnO WGM Optical Resonators

3.3.1 Pre Etch Preparation

While working on the simulations, several samples were fabricated with varying device sizes to help establish the etching solution. A mask with many ring and disk devices was first designed using MEMS L-Edit software. These devices ranged in diameter from 100 – 300 μm in steps of 50 μm. Since expensive e-beam etching is not required for this study, the mask was designed within the capabilities of standard lithography. Images of the mask are shown below in Figure 21.

The mask was then written using a Heidelberg μPG 101 mask writer. Once the mask was written, the photoresist on the mask was then developed using a solution of three parts deionized (DI) water and one part 351 developer for 30 seconds followed by a 30 rinse in DI water. Then the mask was etched using CR-44 Chrome etchant for 90 seconds followed by a 30 second rinse in DI water. The mask was then checked visually under an optical microscope for any defects. Once the mask was ready, samples could be fabricated.

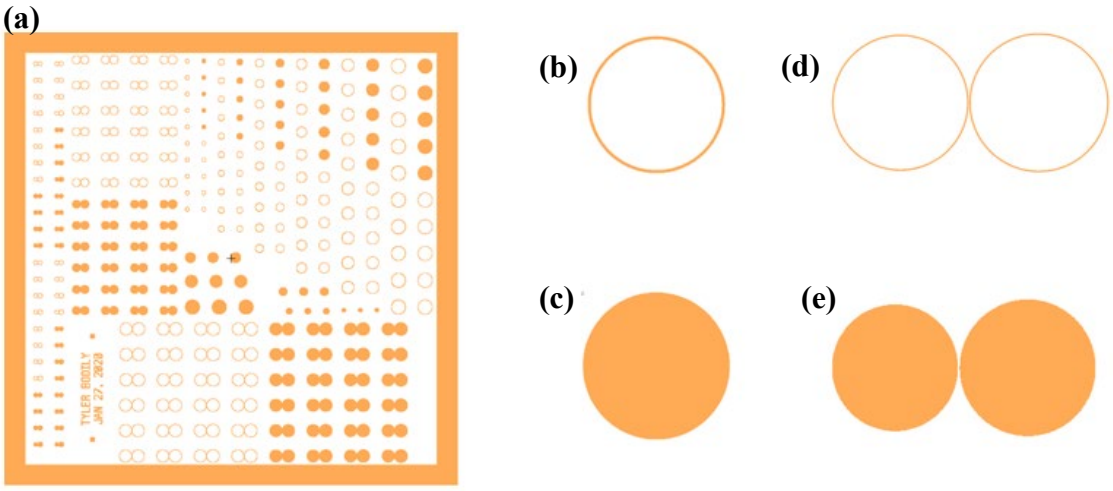

Figure 21. Images of the WGM resonator mask design used in fabrication. (a) Entire layout for a 1.1 cm x 1.1 cm square chip. (b) A single ring resonator with a 200 µm outer edge diameter and 4 µm wide walls. (c) A single disk resonator with 100 µm diameter. (d) Two coupled ring resonators. Both have a wall thickness of 2 µm. The left ring has an outer edge diameter of 200 µm and the right ring has an outer diameter of 208 µm. The gap between them is 1 µm. (e) Two coupled disk resonators with the left disk having a diameter of 100 µm and the right having a diameter of 108 µm. The gap between them is 2 µm.

This process began with ZnO being deposited on either a silicon, or fused silica wafer. The ZnO was deposited by Dr. Kevin Leedy at AFRL/RY. A Neocera Pioneer 180 pulsed laser deposition system with a base pressure of 2.67 x10−5 Pa was used. A KrF excimer laser (Lambda Physik COMPex Pro 110, 248 nm wavelength, 10 ns pulse duration) operated at 30 Hz with an energy density of 2.6 J/cm2 at the target. Depositions occurred at a 200 ◦C substrate temperature, oxygen partial pressure of 3.33 Pa and substrate-to-target distance of 9.5 cm. The target was a 50 mm diameter by 6 mm thick sintered 99.999% pure ZnO ceramic disk. The target and substrate rotated at 40 ◦/s and 20 ◦/s, respectively, and the focused beam followed a programmed scan over the target to achieve uniform film thickness across the 100 mm diameter substrates. These deposition

conditions yielded a nominal growth rate of 0.25 nm/s. A scanning electron microscope (SEM) image and an X-ray fluorescence (XRF) spectrum are shown in Figure 22.

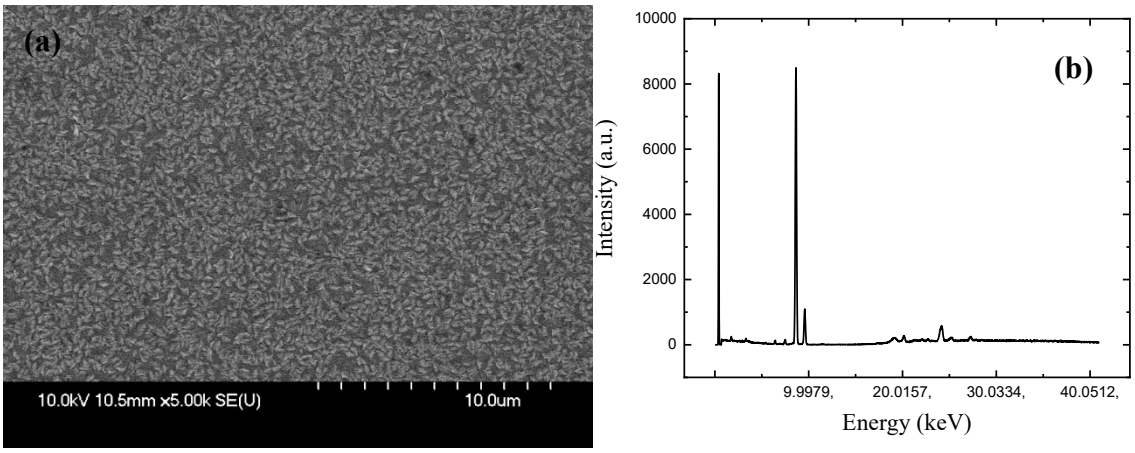

Figure 22. (a) A SEM image of a blank (unetched) sample of ZnO thin film showing large grain boundaries which may be undesirable for the optical phenomenon that is trying to be achieved. (b) The XRF data from the ZnO thin film showing strong K_α and K_β lines. This means the ZnO is pure which is desirable for this study.

From the SEM we can see that the film has noticeable grain boundaries. These are like the grain boundaries shown in Figure 13. The study in that figure showed lasing is possible but it was random lasing due to the grain boundaries. WGM lasing was not explored in that work as it will be in this study. Therefore, these samples were used in the fabrication process even though the grain boundaries may be undesirable for this work. The XRF shows strong peaks and the typical ZnO energies and shows that the film is pure.

Once the films were deposited, the wafers were diced into 1.1 cm x 1.1 cm chips at AFRL/RY. This allowed for many different samples to be fabricated and tested under different conditions. Once the wafers were diced, a chip sample would be prepared for

fabrication. This would begin with a 30 second rinse with isopropyl alcohol to clean the sample. Isopropyl alcohol was used instead of the traditional acetone, methanal, DI water process because ZnO dissolves easily in acetone. After the samples were cleaned a layer of MICROPOSIT S1818 photoresist was spun on at a rate of 4000 rpm to reach an average thickness of 1.8 μm. The device was patterned using the Suss MA6 Mask Aligner System and the mask previously fabricated. The sample was exposed for 3 seconds with 405 nm light. The photoresist was then developed by placing the sample in a 5:1 DI water to 351 developer solution for 30 seconds followed by a 30 second rinse with DI water. The sample was then inspected under an optical microscope for any defects. Once the photoresist was patterned and developed, the samples were ready to be etched.

3.3.2 Wet Versus Dry etching

An adequate and simple etching technique was needed to make the devices as precise as possible to the desired detentions. At first a dry etch using an inductively coupled plasma reactive ion etching (ICP RIE) was tested at AFRL/RY. Dry etching is attractive for this work because of its low isotropic affect which allow for more precise dimensions. However, the wall roughness is much higher than is typically found with a wet etch, which is undesirable for optical devices. Through discussion with Mr. Gary Hughes at AFRL/RY, a dry etch recipe was obtained that would etch at a rate of about 15 nm/min. The etch recipe is shown in Table 4.

Table 6. ICP-RIE Etch Recipe for ZnO

Flow rate of N_2	75 sccm
Pressure	10 mTorr
RIE Power	250 W
ICP Power	1200 W

However, when this recipe was used it was much too harsh for the photoresist and the ZnO. An SEM from the etch is shown in Figure 23.

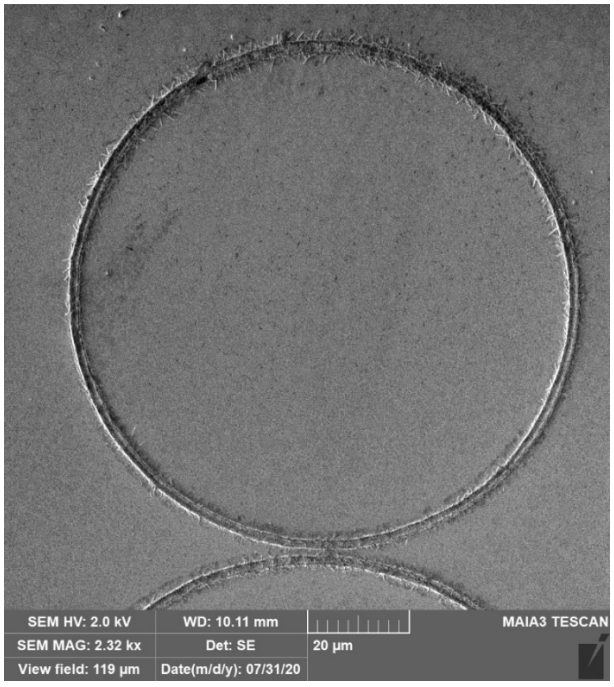

Figure 23. Image of an ZnO ring device after ICP RIE etching. The ring is almost completely etched away and has very rough side walls which would cause scattering to occur. This makes it impossible to use for this work.

As can be seen from this image, the devices were almost completely eaten away. This could have been the result of too long of an etch time, or because of an improper gas balance. The reason could have been explored and tested further, however, the logistics of using the AFRL/RY ICP RIE to go through these many tests made it difficult to purse this course of action, especially when wet etching was readily available in the clean room at AFIT.

3.3.3 Ammonium Chloride Etch Test

Wet etching is a desirable technique because it is very cost effective and is easily done in any clean room. The drawback to wet etching is its isotropic properties that produce quite a bit of lateral etching in devices. This can make it difficult to get precise sizes and sharp features in devices. For this purpose, it was important to find an etching solution that would minimize the lateral etch effect. Several solutions have been studied for etching ZnO, including hydrochloric acid (HCl), nitric acid (HNO_3) and phosphoric acid (H_3PO_4) [78], [81], [82]. However, the etching wasn't uniform or consistent enough to be feasible for this study [79]. Through further research, Ammonium Chloride (NH_4Cl) was found to be the most feasible option for use in the AFIT clean room. However, it was difficult to replicate the etch rates found in [78], [79]. Because of this it was decided by our lab group that were all using ZnO in our various research, that we would conduct a Design of Experiments (DOE) analysis to characterize the optimal concentration and etch rate. The experiment was run in 2 batches. The first batch was a single-factor two-level full factorial design with three replicates. The second batch was a three-factor two-level full factorial design. Each of the samples for each run was a 1.1 cm x 1.1 cm square

prepared in a similar fashion to the preparation of ring and disk samples discussed above. The samples were cleaned and had MICROPOSIT s1818 photoresist spun on at a rate of 4000 rpms. From there a grid of 1 mm x 1 mm squares was patterned and developed to prepare for etching. The samples were then etched at different concentrations, temperatures, and agitation levels. From the results we were able to conclude that the significant factors are concentration and temperature, and we were able to model the etch depths as shown in Figure 24.

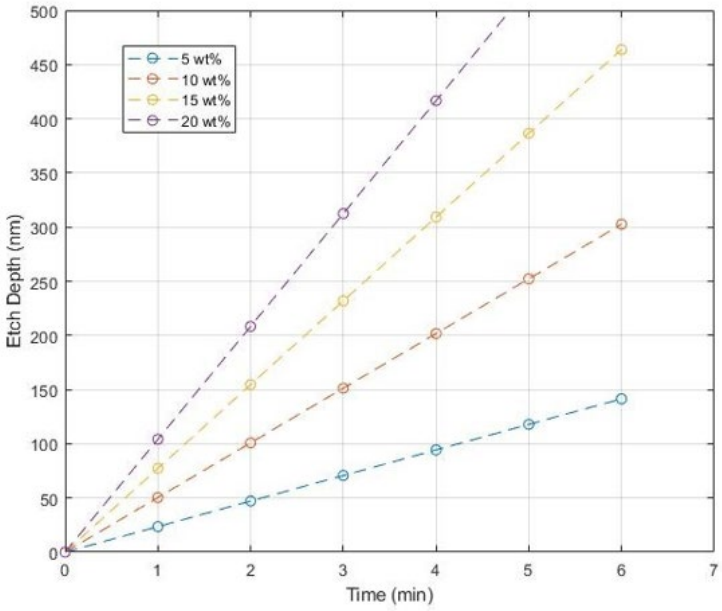

Figure 24. Model etch rates of several concentrations of NH_4Cl at room temperature with mild agitation.

From the results above it was decided that the 20% solution at room temperature with mild agitation would be most useful for this project.

3.3.4 Etching using Ammonium Chloride.

Once the ammonium chloride etch process was characterized, it could be used to etch the devices. The aqueous NH_4Cl solution was made by mixing 99.5% pure lab grade powder NH_4Cl into DI water. The solution was first stirred and then but into a 5 minute hypersonic bath to complete the mixing. The prepared sample was then etched for the appropriate time according to the results above. Once the devices were etched, the photoresist was removed using an oxygen plasma so that the ZnO would not be attacked by any chemicals that could be used to remove the photoresist. A sample would be placed in the Anatech USA-SP 100 plasma asher for 90 min at 200 W. Once the photo resist was removed the samples were examined under an optical microscope and SEM to see if the etch was successful. Some examples of the images gained from the optical microscope are shown in Figure 25. Some SEM images are shown in Figure 26.

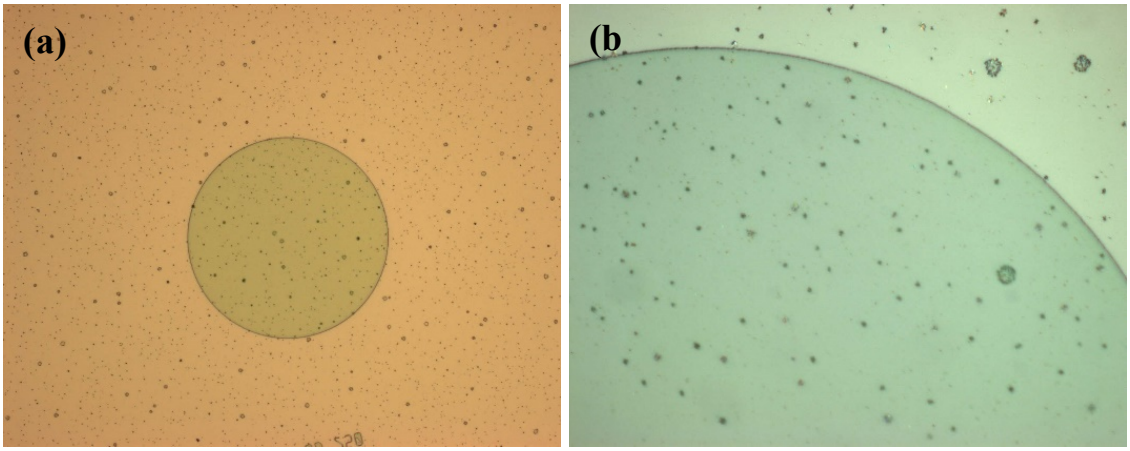

Figure 25. (a) Optical microscope image of a WGM device etched with NH_4Cl. (b)The same disk zoomed in on an edge. The edge is very smooth which is very desirable for this study.

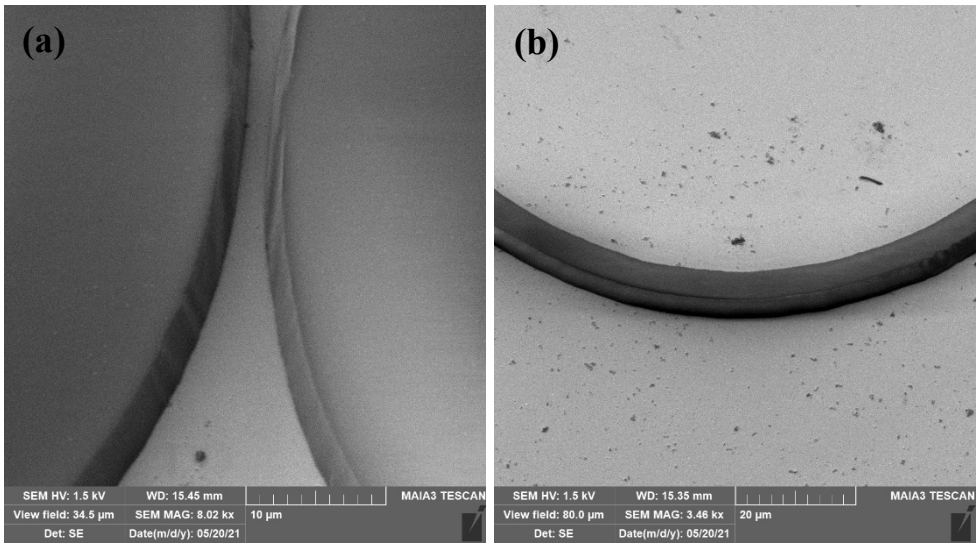

Figure 26. (a) A SEM image zoomed in on the gap between two coupled disks showing a smooth wall and a complete etch between the disks. (b) A SEM image of a ring zoomed in to show a smooth wall. Both images confirm a successful etch using NH_4Cl.

3.4 Experiment Set Up

Once the devices were etched, they were ready for testing at AFRL/RY. Two different lasers with two slightly different experiment set ups were used to excite the devices. A continuous wave (CW) laser was used to excite and trap light within the WGM device in both set ups. In the first set up, the pump beam passed through a bandpass filter and was focused through an optical lens onto a device on the sample chip. The sample was either perpendicular to the excitation laser or would vary between 90º and 45º. The emission was then focused into a spectrometer using another optical lens. An example of the test set up is shown in Figure 27.

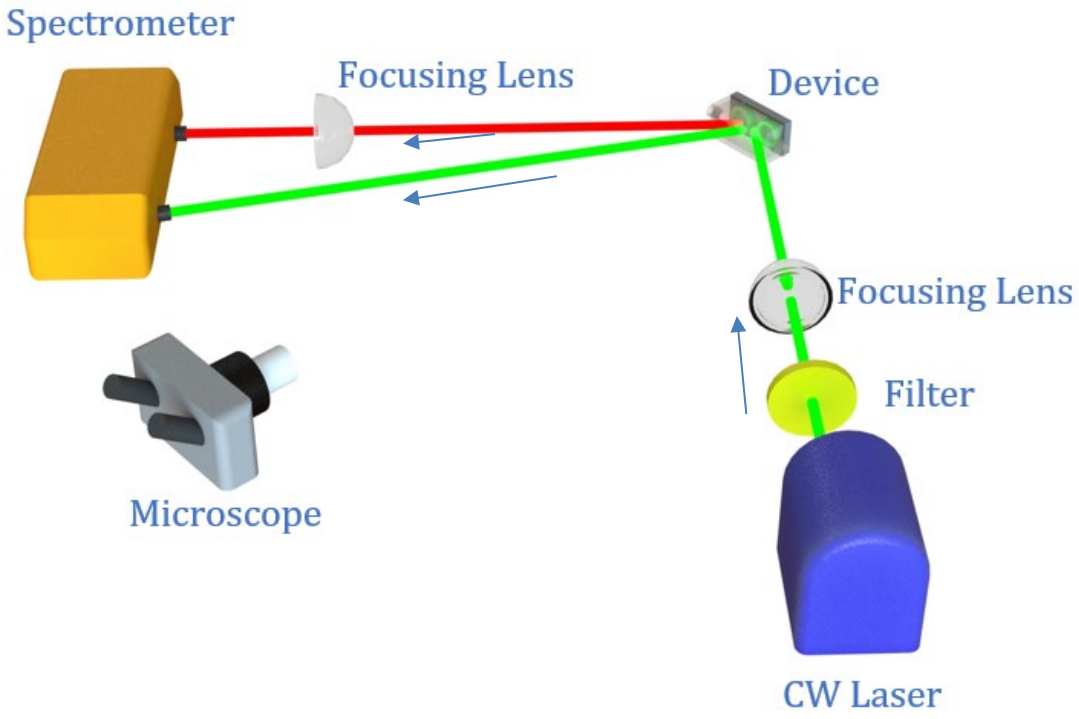

Figure 27. Experimental set up for testing the WGM devices. The green line represents the laser light from the continuous wave pump laser. The red is the emission from the device.

Two different pump lasers were available for excitation in testing. Using different pump lasers was desirable to compare responses of the devices and see if one system had a better response. The first was a Kimmon IK Series Helium-Cadmium (He-Cd) 325 nm laser. The beam was focused to approximately 5 µm in diameter and had a power output of about 3 mW at the device. A SPEX 1250M Spectrometer with a 2400 grating was used to detect the laser emission from the devices. A picture of the setup is shown in Figure 28.

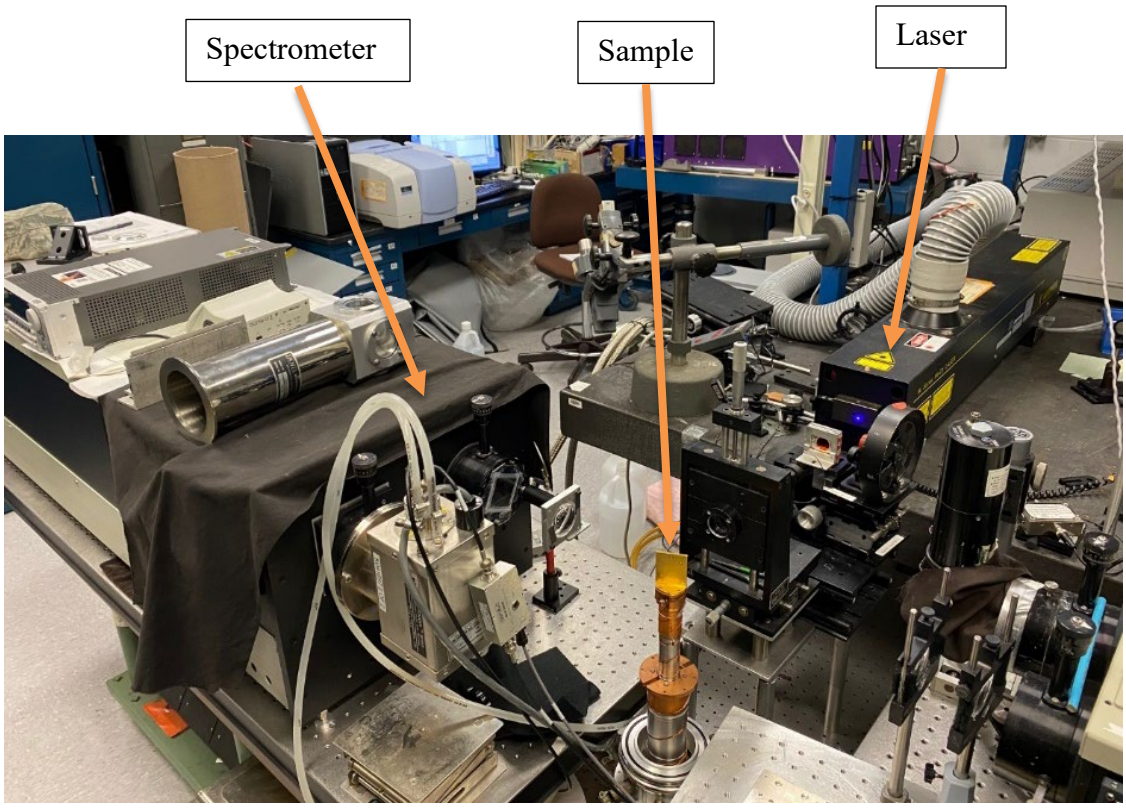

Figure 28. A Picture of the actual experimental set up using a Kimmon Laser as the pump laser.

If the laser emission is weak, this set up could also include a fiber optic cable to help with the emission detection. In this case a fiber cable was added between the sample and the spectrometer. One end of the cable had a focusing lens and was focused close to the edge of the device to detect laser emission from the side of the device. The other end of the cable was then focused into the spectrometer for detection. A picture of this set up is shown in Figure 29.

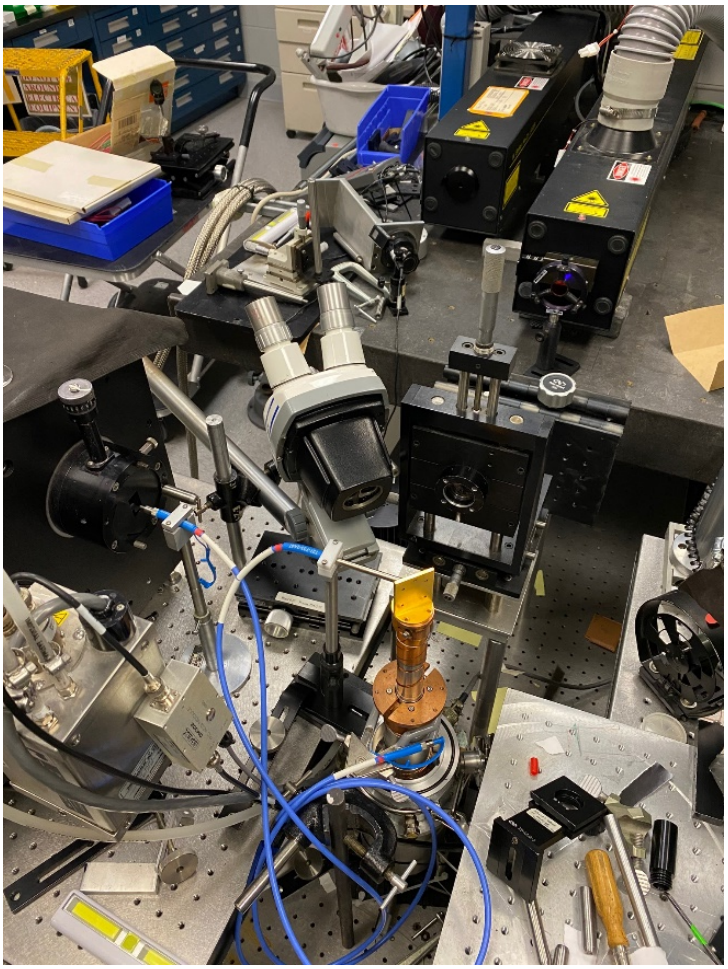

Figure 29. Experimental set up for testing the WGM devices with a fiber optic cable inserted between the sample and the spectrometer. This helps to detect the laser emission from the device.

The third pump laser available was part of the Renishaw inVia Raman Microscope system. This system also uses a He-Cd 325 nm laser. The beam size could be set anywhere between 1-100 µm and had an output power of 5 mW. This system had the same basic configuration as the first set up, with a few differences. Those differences can be seen in the schematic and picture shown in Figure 30. The sample could be placed at 90º to the excitation laser or at an angle of about 30º with an aluminum mount.

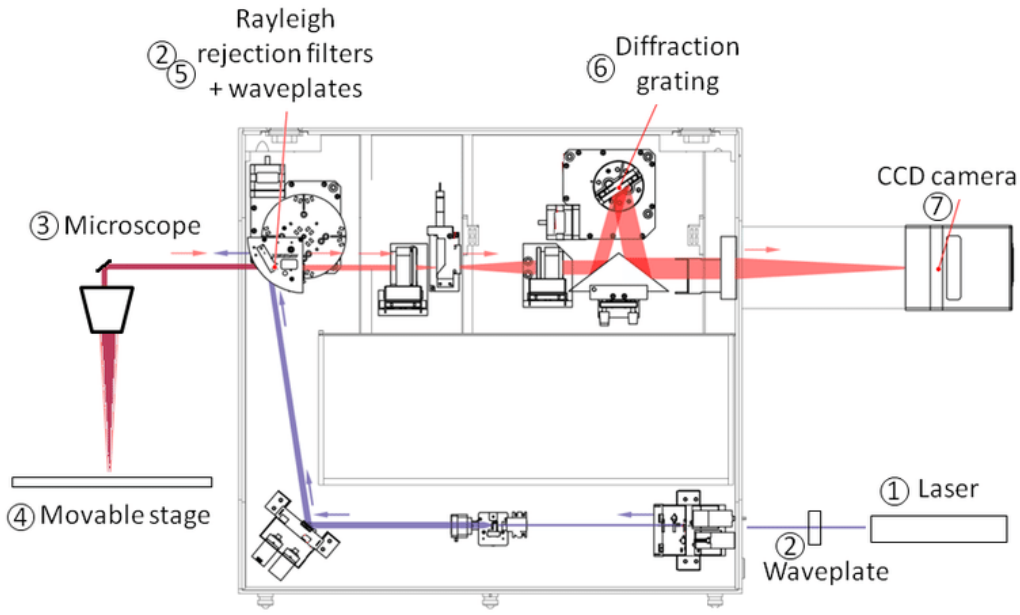

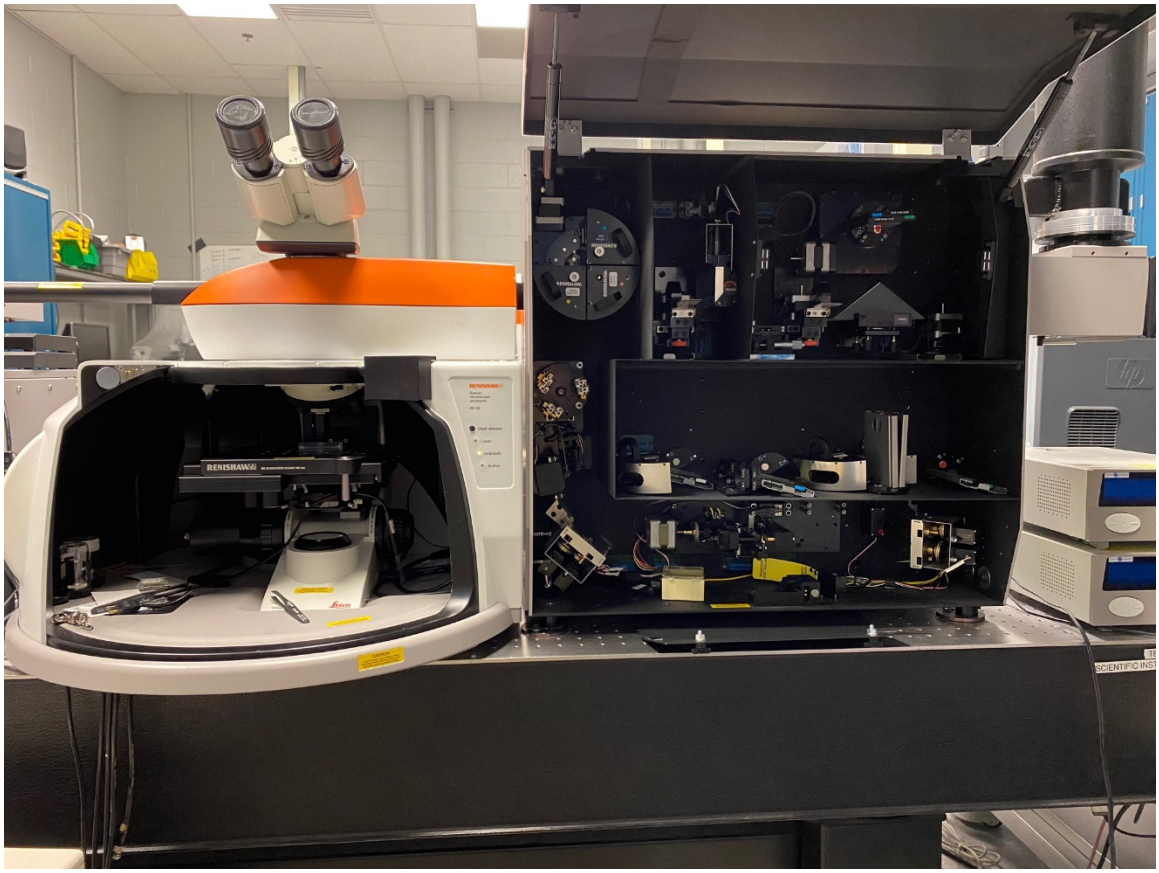

Figure 30. Schematic [83] and picture of the Renishaw inVia Raman Microscope.

Both pump lasers can give a clear photoluminescence (PL) curve, as well as show possible laser emission from the ZnO devices.

3.5 Summary

The methodology behind testing ZnO WGM resonators consisted of three main parts: simulation of the devices, fabrication, and experimentation. The simulations helped to define the fabrication process. They also helped show that the actual devices fabricated using standard cleanroom techniques were able to support lasing. The experimentation set up allowed for several different avenues for the testing of the devices to determine which one was most successful.

IV. Analysis and Results

4.1 Chapter Overview

This chapter will go through the data that was collected for each sample tested on each of the three lasers. It will begin with the first samples tested with the Kimmon IK Series Helium-Cadmium (He-Cd) 325 nm laser. The data collected from the Renishaw inVia Raman Microscope will then be discussed. Further samples of larger diameter were also tested using both lasing systems with a few devices even tested at low temperatures.

4.2 Results from the Kimmon IK Series Helium-Cadmium (He-Cd) 325 nm Laser

Devices were first tested using the Kimmon IK Series Helium-Cadmium (He-Cd) 325 nm laser in the same set up that is shown in Figure 28 above. Before any tests on WGM devices were done, the photoluminesce (PL) was taken on blank (pre-fabricated) ZnO samples that were deposited on silicon and fused silica. This helped us to know where to focus our scans when looking for laser emission since it will happen around the PL curve. The PL curves are shown in Figure 31.

After the PL data was collected and analyzed, the first ZnO WGM devices tested were about 450 nm thick with diameters ranging from 100 μm to 300 μm. They were on a silicon substrate with about a 100 nm thick layer of tungsten between the silicon and the ZnO. It was decided the disks would be tested first since they had a big enough area of ZnO for the laser to easily focus on. The first tests were to confirm that we could duplicate the PL data that we had seen above. Those results are shown in Figure 32.

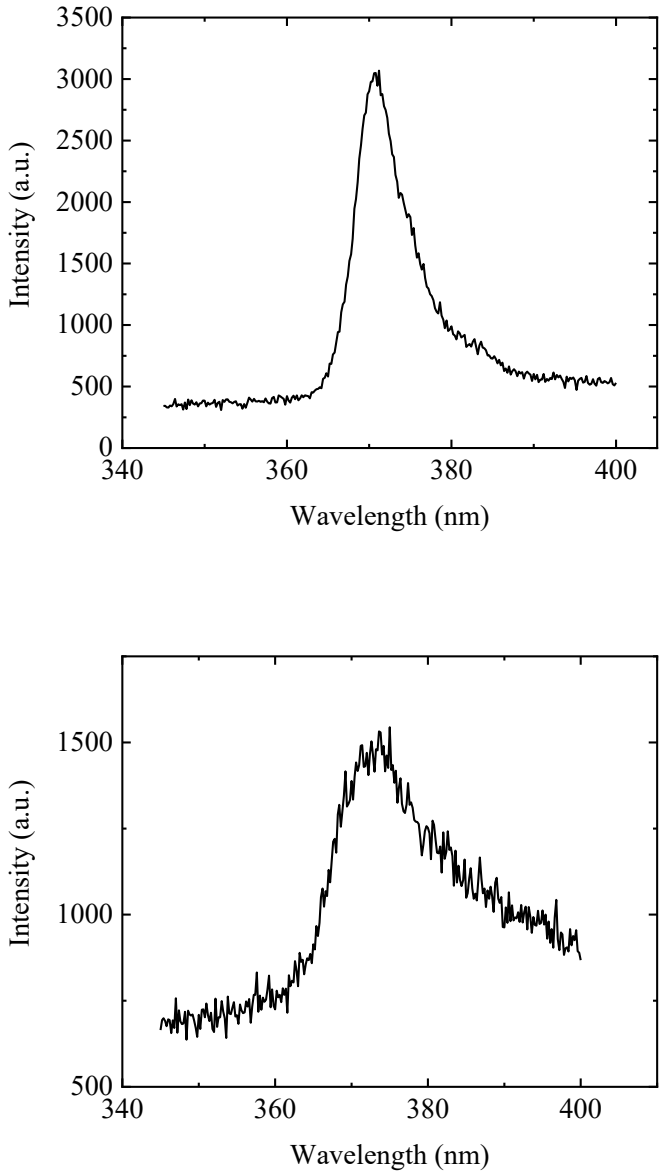

Figure 31. PL emission from ZnO samples taken with a laser intensity of 3.82 kW/cm^2. The top one is from approximately 900 nm of ZnO on fused silica. The bottom is about 200 nm on silicon.

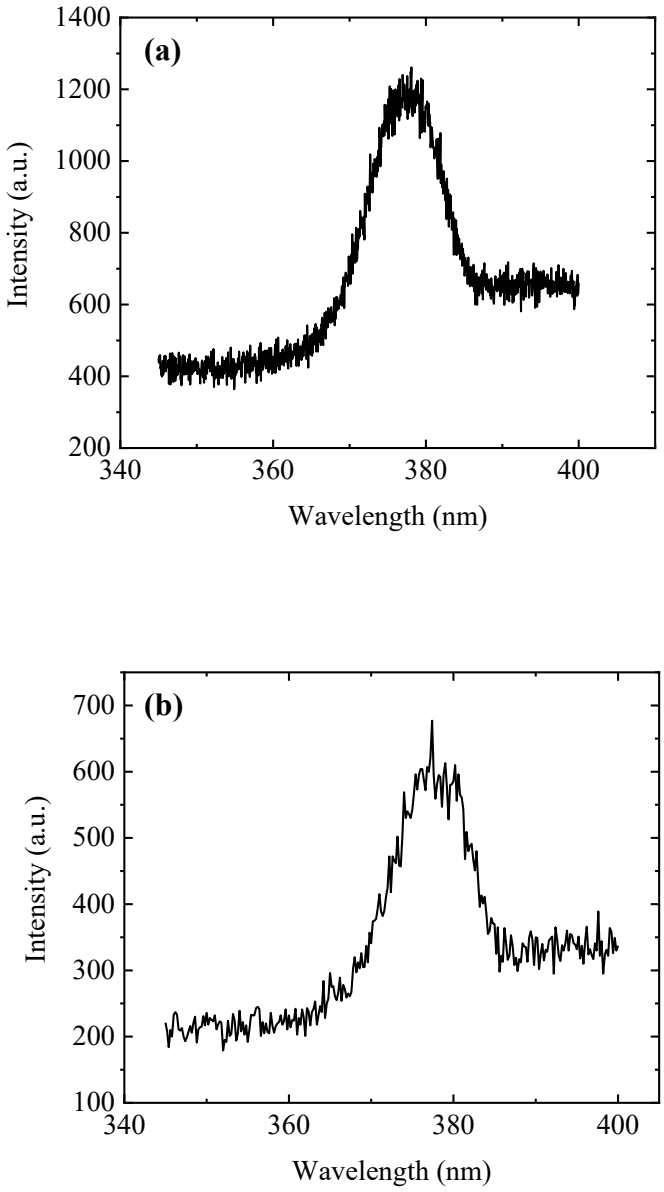

Figure 32. (a) A PL curve of a 300 μm disk WGM taken with a pump intensity of 1.78 kW/cm^2. (b) A PL curve of a 150 μm disk WGM taken with a pump intensity of 1.78 kW/cm^2.

Based on the results above, it is shown that there is enough ZnO to see a similar PL curve, and should be able to see WGM laser emission. From here it was decided that

several of the disks of varying sizes would be tested to see if any of them emitted laser light. The results of one of these tests are in Figure 33.

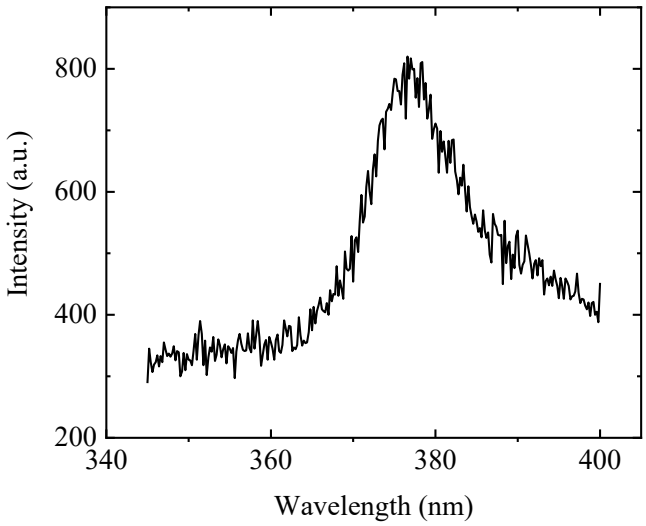

Figure 33. More data collected by the He-Cd 325 nm laser with a pump intensity of 3.44 kW/cm^2 on a 300 µm diameter disk showing the same PL curve found before.

After many tests on 4 different samples, the same PL curves were collected but none of them showed any lasing peaks. More examples of these can be found in Appendix A. It was quite unexpected that no lasing would be observed since it was quite easily observed in other research [66], [67], [85]–[88], [68]–[74], [84]. It was then hypothesized that the beam intensity of this laser may not be strong enough. The maximum power measured from this laser was about 3.1 mW and the minimum was about 2.7 mW. The beam diameter was estimated to be about 5 µm. At the highest power output of 3.1 mW, this would give an intensity of 15.8 kW/cm^2 which is at the very low end of lasing thresholds observed in other ZnO lasers [74]. Since even the slightest error

in estimation would mean that the lasing threshold would not be met, it was decided to try a more powerful laser.

4.3 Results from the Renishaw inVia Raman Microscope

The only other laser available at the time was the Renishaw inVia Raman Microscope at AFRL/RY. This system had a slightly higher power output of 5 mW but the beam size could accurately be focused to 1 µm. This gave an intensity of 636.6 kW/cm^2 which is well within the range of other reported lasing thresholds. The devices were then excited using the setup show above in Figure 30. The results are shown below in Figure 34.

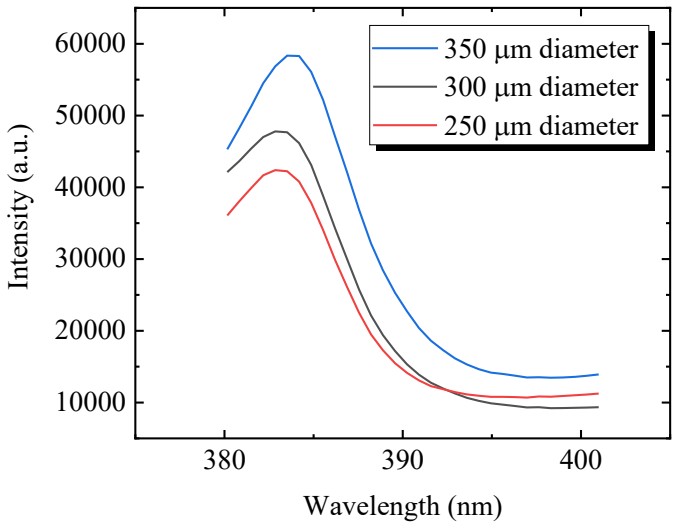

Figure 34. PL emission of three WGM disks ranging in diameter from 250 µm to 350 µm. PL emission is shifted to the right when compared to the other results, but this is most likely due to the increased intensity. No lasing peaks were detected.

These results have a much greater intensity and have a slightly shifted peak compared to the PL curves from the first laser. However, there still are no lasing peaks, despite the

higher intensity laser. This could be due to the small beam size. If a disk diameter of 200 µm is focused on, then the excited area is only 1/40,000 of the total disk area. It was then decided to try and excite the devices using the same set up but with the beam diameter expanded to 100 µm. This would allow for a greater area of the device to be excited, but it would bring the intensity down below the past observed lasing thresholds of ZnO to 63.6 W/cm^2. Even though the intensity is low the data in Figure 33 does show that the PL response is consistent. Again, the only difference is in the intensity count.

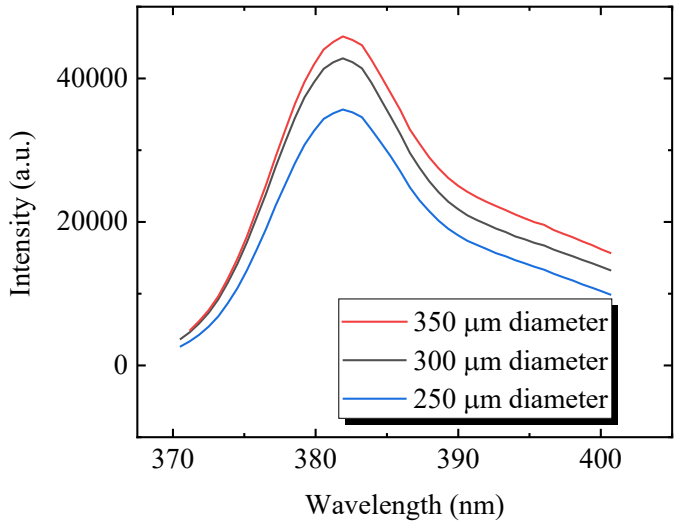

Figure 35. Results of exciting three WGM disks ranging in diameter from 250 µm to 350 µm with an expanded beam diameter of 100 µm and intensity of 63.6 W/cm^2. Similar PL emission is seen without lasing peaks.

These graphs were each taken with a 150 grating which may not give the necessary resolution to see the narrow lasing peaks that were expected. The measurements were then taken again, though this time with a 2400 grating. The results of these are shown in Figure 36.

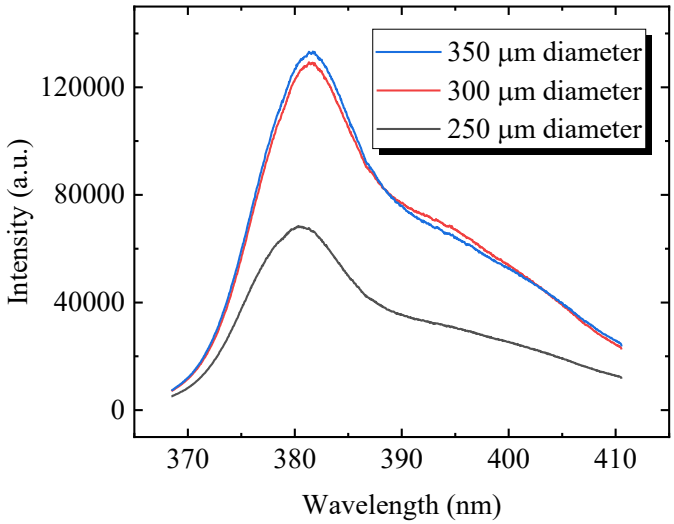

Figure 36. Results of exciting WGM disks ranging in diameter from 250 µm to 350 µm taken with a 2400 grating. Similar PL emission is seen without lasing peaks.

These results give a much higher resolution that would be able to show the narrow lasing peaks that were expected. However, as can be seen, the peaks are not present.

4.4 Testing Larger Diameter Devices with the Kimmon and Renishaw Systems

Since the higher power laser and the higher resolution did not produce any lasing emission, it was decided that new samples would be designed, fabricated, and tested. There were two wafers, one silicon and the other fused silica, that each had 810 nm of ZnO deposited on them with no extra layer of metal. These wafers were diced into 1.1 x 1.1 cm square chips. The devices fabricated on these new samples had larger diameters. Their diameters ranged from 200-500 nm increasing by 50 nm steps. Larger devices were chosen to minimize the amount of light scattering as the captured laser light traveled

around the WGM resonator. These larger devices were tested with both the Kimmon and Renishaw pump lasers.

Before the devices were etched and tested, a PL scan was done on blank samples of the ZnO using both the Kimmon and Renishaw pump lasers. The results can be seen in Figure 37 below. These PL curve agrees with the previous PL curves taken of the ZnO samples used in this study. This curve also serves as a good reference for the future tests on the WGM devices.

Once the PL data was acquired, the large devices were tested using the Kimmon pump laser. Again, the disk devices were tested first since there was a larger area for the beam to focus on. The devices were also tested at least two times with the beam focused on the center and then focused closer to an edge. An example is shown in Figure 38, with the more of the data presented in Appendix A. As is seen from this figure, the same PL curve is seen but no lasing was detected. The samples were then tested using the Renishaw pump laser.

The larger disks were also tested using the Renishaw pump laser. The results of a few devices on both silicon and fused silica are shown in Figure 39. These results show the same PL curve of ZnO that has been observed throughout the testing.

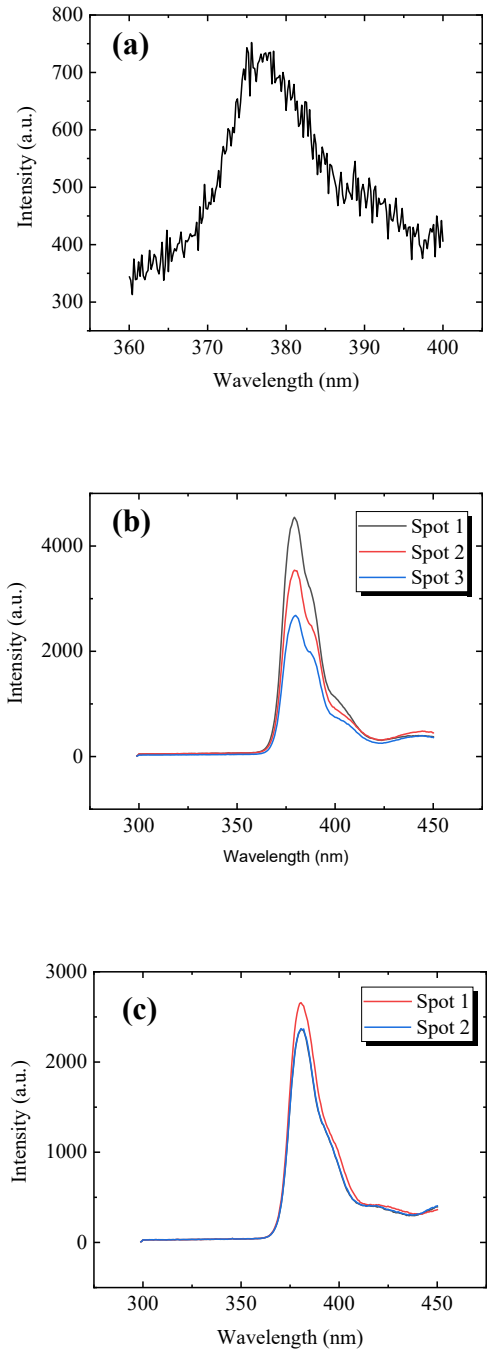

Figure 37. (a) PL emission of 810 nm of ZnO on a fused silica substrate taken with the Kimmon pump laser with an intensity of 3.82 kW/cm^2. (b) PL emission of three different spots on 810 nm of ZnO on a silicon substrate taken with the Renishaw pump laser with a pump intensity of 63.6 W/cm^2. (c) PL emission of two different spots on 810 nm of ZnO on a fused silica substrate taken with the Renishaw pump laser with a pump intensity of 63.6 W/cm^2.

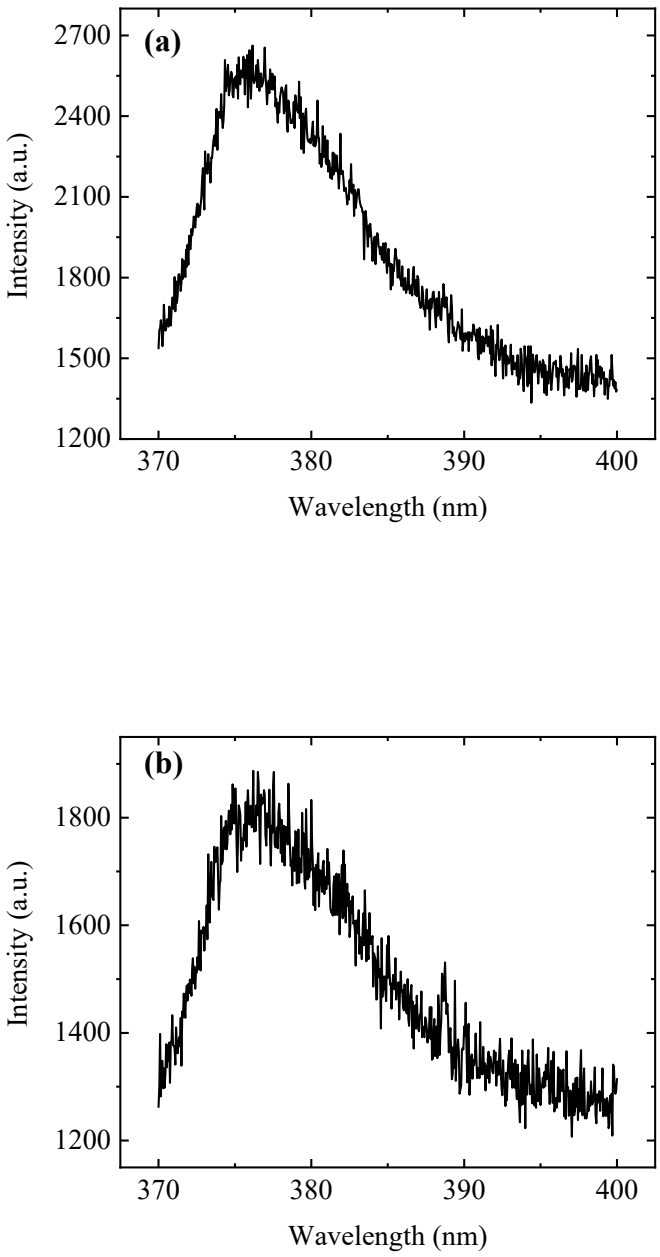

Figure 38. (a) Data collected from pumping the center of a 450 μm diameter disk on fused silica. (b) Data collected from pumping the same disk along an edge. Both were taken with a pump intensity of 3.82 kW/cm^2.

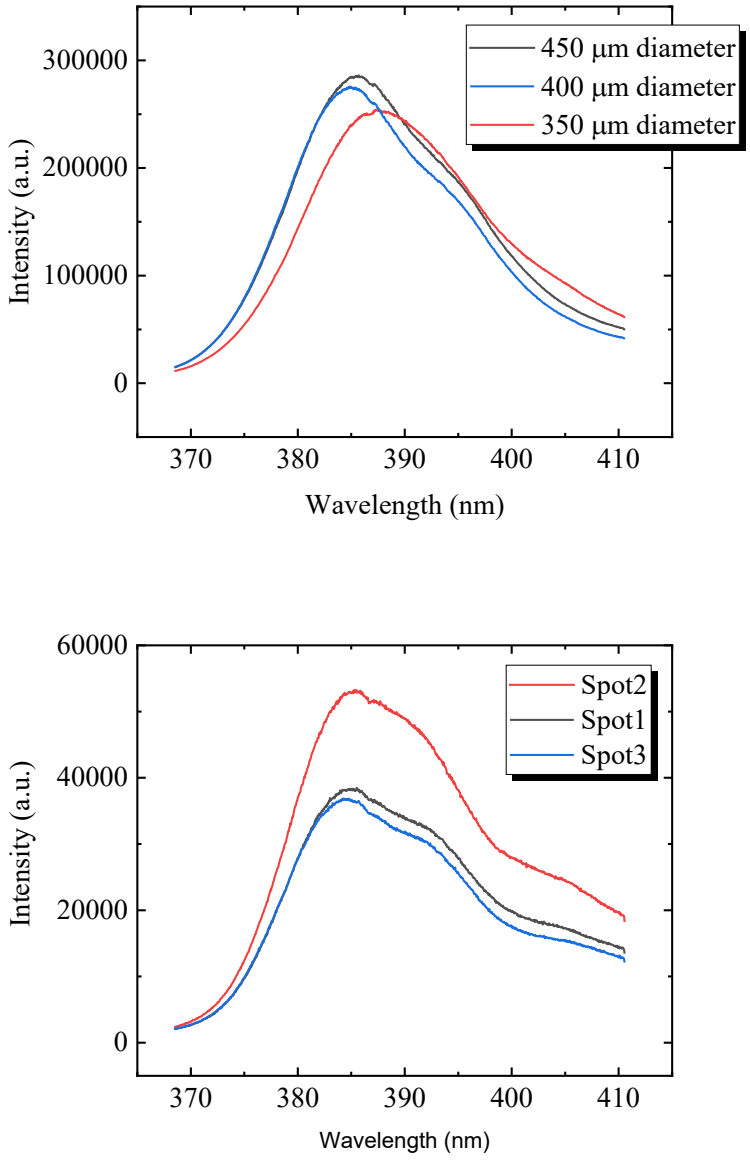

Figure 39. (a) Data taken from disk with diameters ranging from 350-450 µm on silicon. (b)Data taken from three different spots on a 500 µm diameter disk on fused silica. Data was gathered using the Renishaw system with a 2400 grating and beam size of 1 µm.

It has been shown that ZnO lasing has occurred at low temperature [89], so the next tests were done after the samples had been cooled. The Renishaw pump laser has the capabilities to cool samples as low as -174 °C using liquid nitrogen. The samples are

placed inside an enclosed stage where the liquid nitrogen in used to cool the sample. The tests were run with a 2400 grating and beam size of 1 µm. The results can be seen in Figure 40.

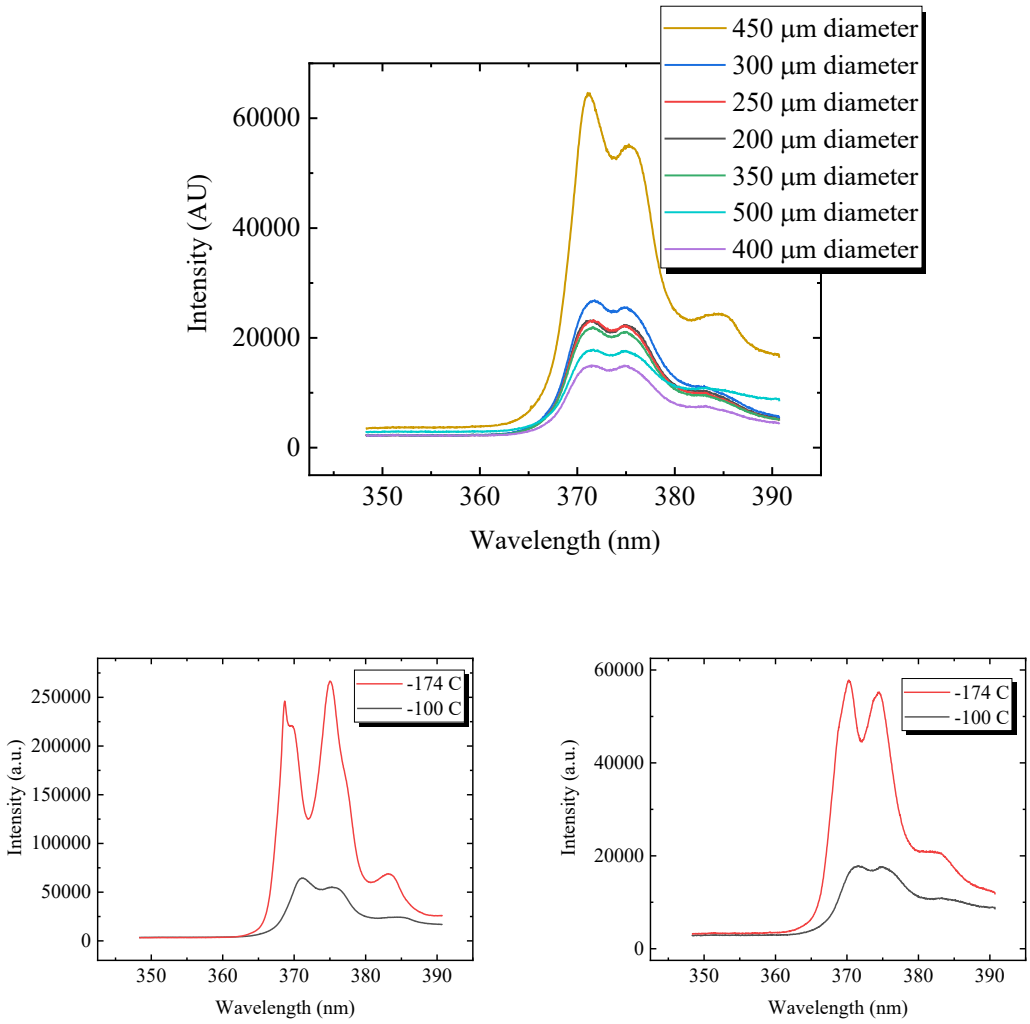

Figure 40. (a) PL data from disks with diameters ranging from 200-500 µm with the diameter increasing in 50 µm steps. All this data was collected at -100 ºC. (b) PL data taken at -100 ºC and -174 ºC of a 450 µm diameter disk. (c) PL data taken at -100 ºC and -174 ºC of a 500 µm diameter disk.

It is interesting to note that the standard PL curve at low temperature widens and begins to split into two peaks at -100 ºC. By -174 ºC the two peaks become very distinct.

Similar data has been found in [90]–[92]. This phenomenon is attributed to the semiconductor properties of ZnO. At low temperature it becomes easier for electrons to move between the valence and conduction band and so the emission peaks become sharper. However, there are still no lasing peaks observed.

The final tests were done using the Renishaw pump laser with the samples angled at about 30°. These tests were done at room temperature since the stage device used to angle the samples would not fit inside the cooling stage. The results of these tests are shown in Figure 41.

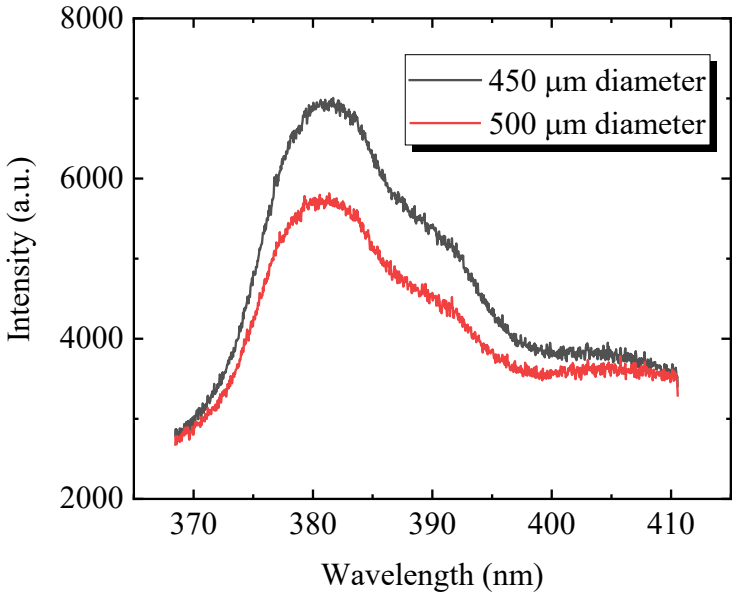

Figure 41. Results from the Renishaw system with the devices angled at 30°. The resulting PL curve is like other observed curves with the only difference being a lower intensity due to the angle change.

Unfortunately, the results were the same as the previous tests done at room temperature with the samples perpendicular to the incoming laser light. It was determined

that the pump lasers used for testing were not sufficient to excite the ZnO WGM resonators enough to achieve lasing. Both experimental set ups were not able to reach the desired intensity to reach the lasing threshold of ZnO with a large enough beam size to excite all or most of the WGM resonators. The grain boundaries shown in Figure 22 may also inhibit the lasing in the WGM resonators but until the devices are excited with a sufficient laser, this cannot be confirmed.

4.5 Summary

Many different sized WGM devices were tested using both the Kimmon and Renishaw systems. At room temperature, each device showed the standard PL curve of ZnO but no lasing peaks were ever observed. When the samples were cooled using liquid nitrogen on the Renishaw system, there was a split in the PL curve but again no lasing peaks.

V. Conclusions and Recommendations

5.1 Conclusions of Research

This study has focused on the design and fabrication of ZnO optofluidic laser elements. The design was simulated using COMSOL Multiphysics® Modeling Software to confirm the calculated dimensions of the WGM resonators and the coupling distance between two devices. The simulations showed that coupling was possible at greater distances when liquid with a high refractive index was used between the devices. This is significant because an expensive and relatively slow dry etching technique is needed fabricate devices with very small, precise spacing. However, with the introduction of liquid, a simple and inexpensive wet etching technique can be used to make the devices since the spacing can be much greater. The fabrication of the devices was successful using standard cleanroom procedures and etching with an ammonium chloride wet etch. This solution proved especially useful in fabricating disk devices. It is more difficult to get consistent results with ring WGM devices because of the lateral etch that is characteristic of wet etching. Once the design and fabrication were successful, the devices were tested using two different pump lasers to see if lasing would occur. However, no lasing was observed in any of the devices. Recommendations for future work is outlined below.

5.2 Recommendations for Future Research

This introductory research can be used as a foundation for many different areas of future research. Some possible paths forward include:

- Using a more powerful laser that can reach a high lasing threshold in the order of 10^2 kW/cm^2, and a beam size of at least 100 µm. This should easily reach the lasing threshold of ZnO and excite a large enough area of the device to see lasing.

- Once lasing is seen on the devices, test different liquids and flow rates over the devices to see how the lasing peaks are affected an example for a liquid case is shown in Figure 42. This can be connected to a programmable syringe pump for easy control of flow rate.

- Further study of other wet etch solutions that may produce less lateral etch.

- Further study and experimentation of the width of ring devices needed to consistently survive the wet etch process.

- Further study and testing of possible dry etching techniques. This could include simpler, and therefore less expensive, recipes, as well as the appropriate photoresist needed to get a successful etch.

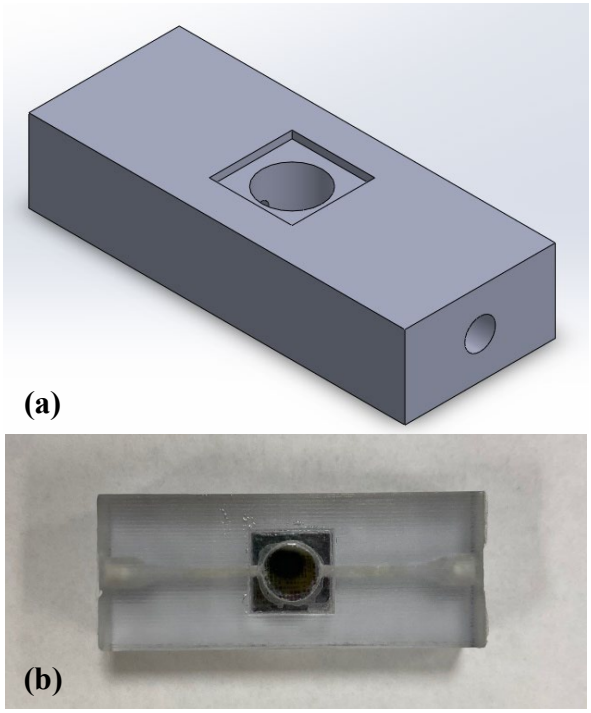

Figure 42. (a) SolidWorks rendering of a fluidic chamber. (b) Picture of an actual 3D printed chamber with sample chip installed.

Appendix A: Supplemental Graphs

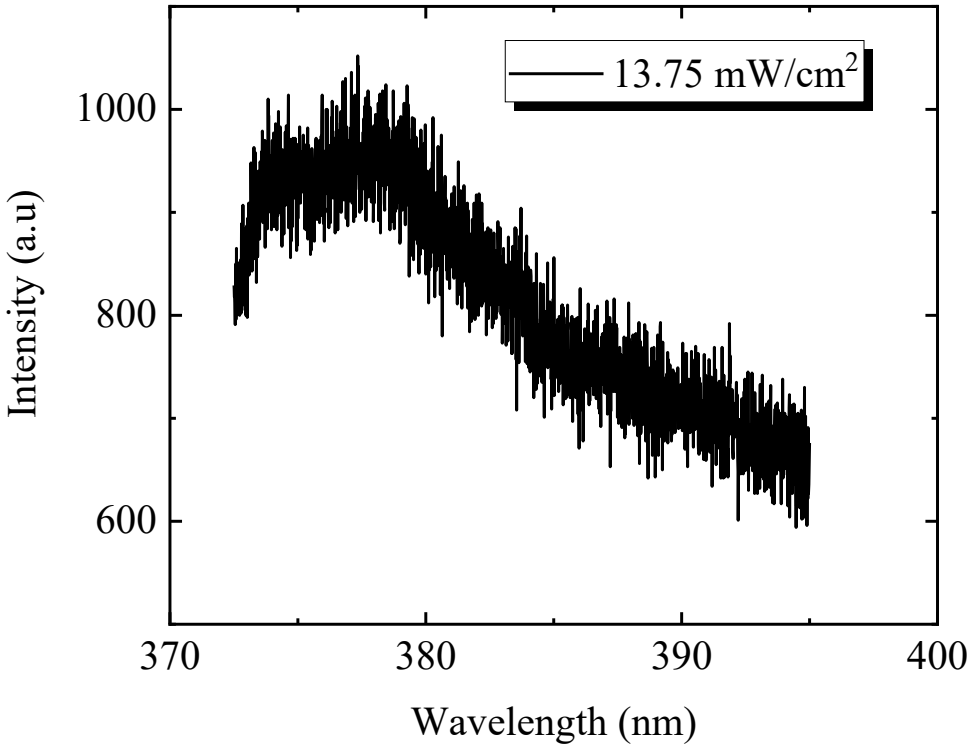

Figure 43. PL curve from a 300 μm diameter, 500 nm thick disk. Pumped by the Kimmon Laser.

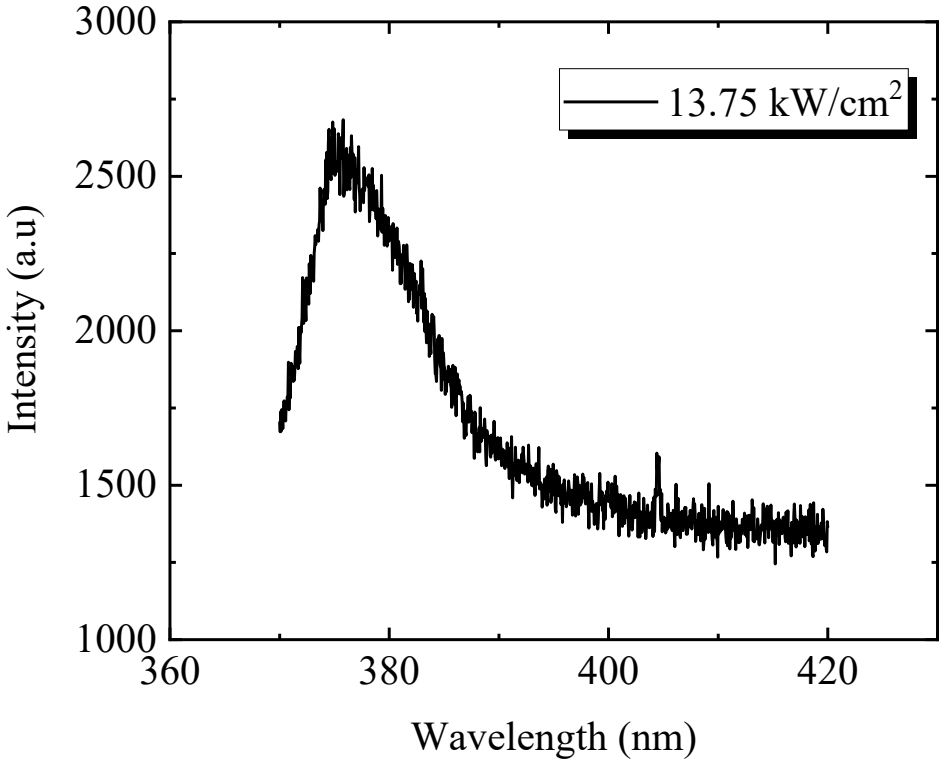

Figure 44. PL curve from a 250 μm diameter, 500 nm thick disk. Pumped by the Kimmon Laser.

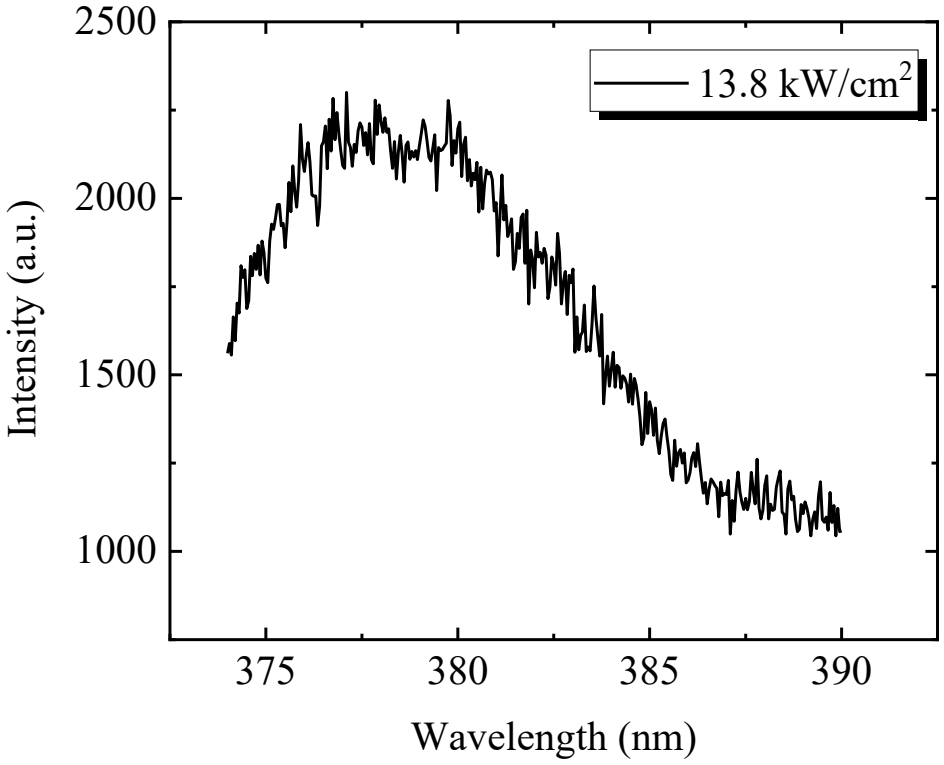

Figure 45. PL curve of a 400 μm diameter, 810 nm thick disk.

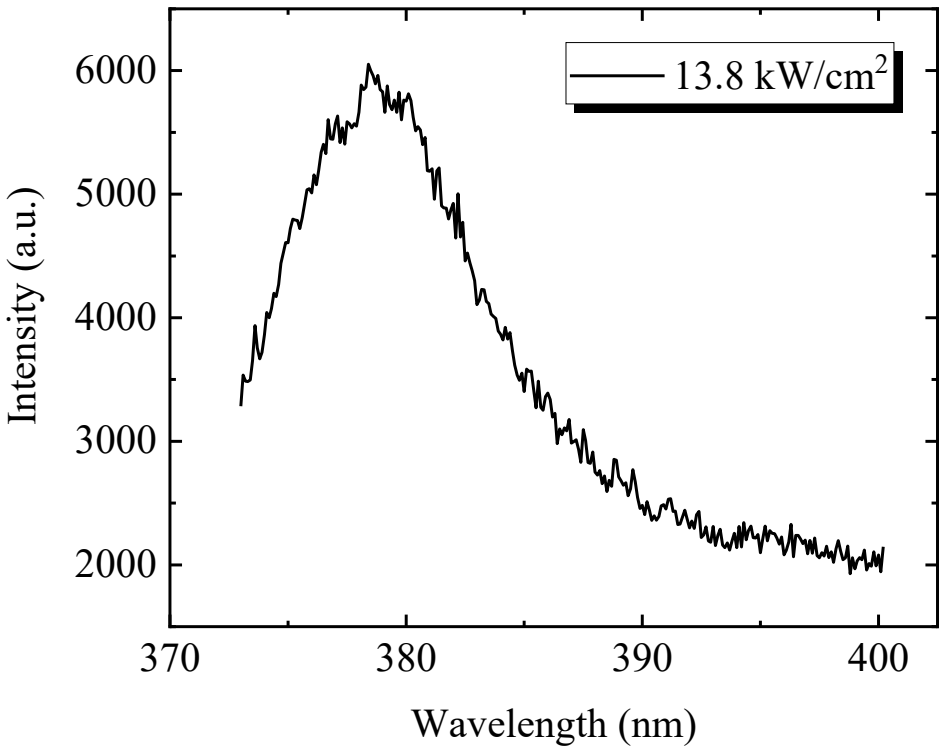

Figure 46. PL curve of a 350 μm diameter, 810 nm thick disk.

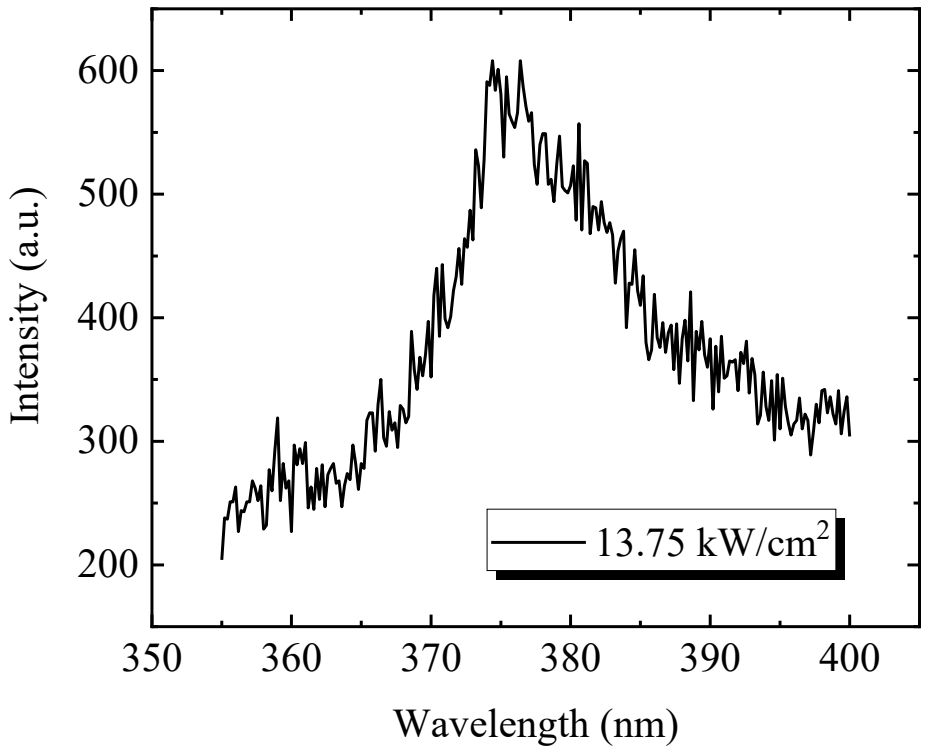

Figure 47. PL curve of a 350 μm diameter, 500 nm thick disk. Pumped by the Kimmon Laser.

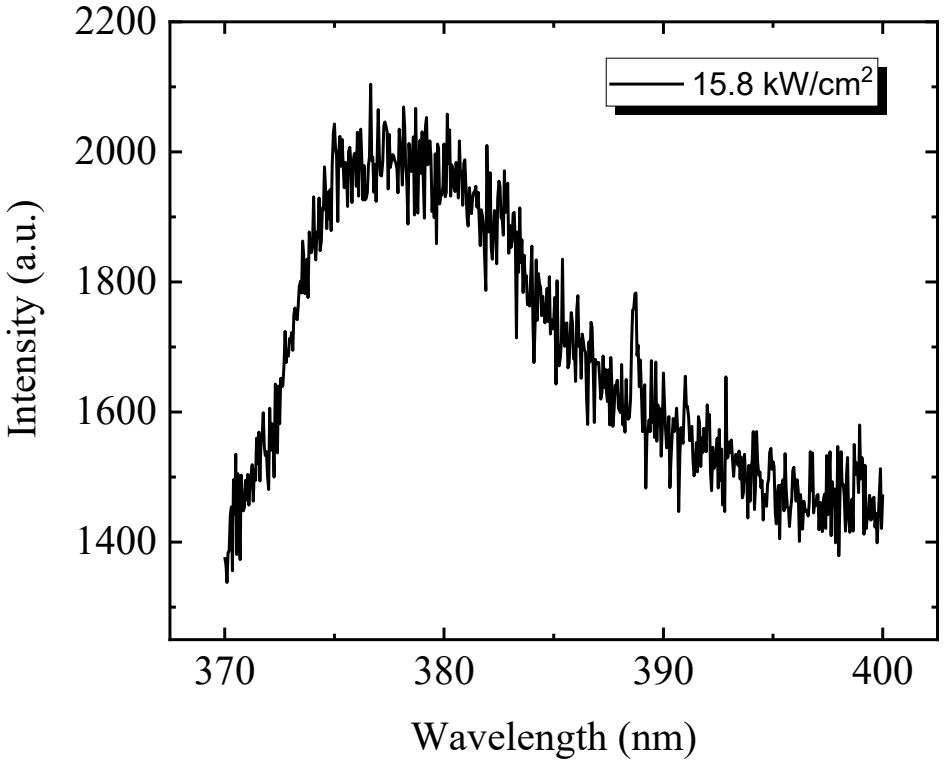

Figure 48. PL curve of a 100 μm diameter, 500 nm thick disk. Pumped by the Kimmon Laser.

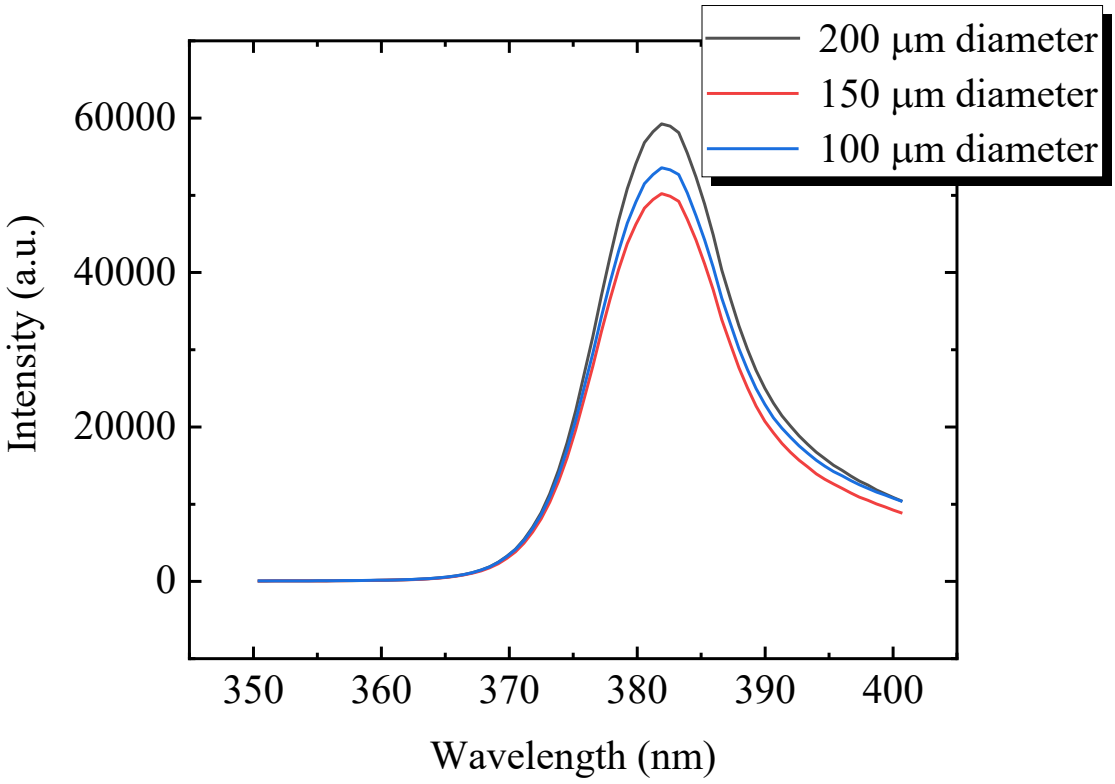

Figure 49. PL emission from disk ranging in diameter from 100 – 200 µm. Taken with the Renishaw system with beam diameter expanded to 100 µm.

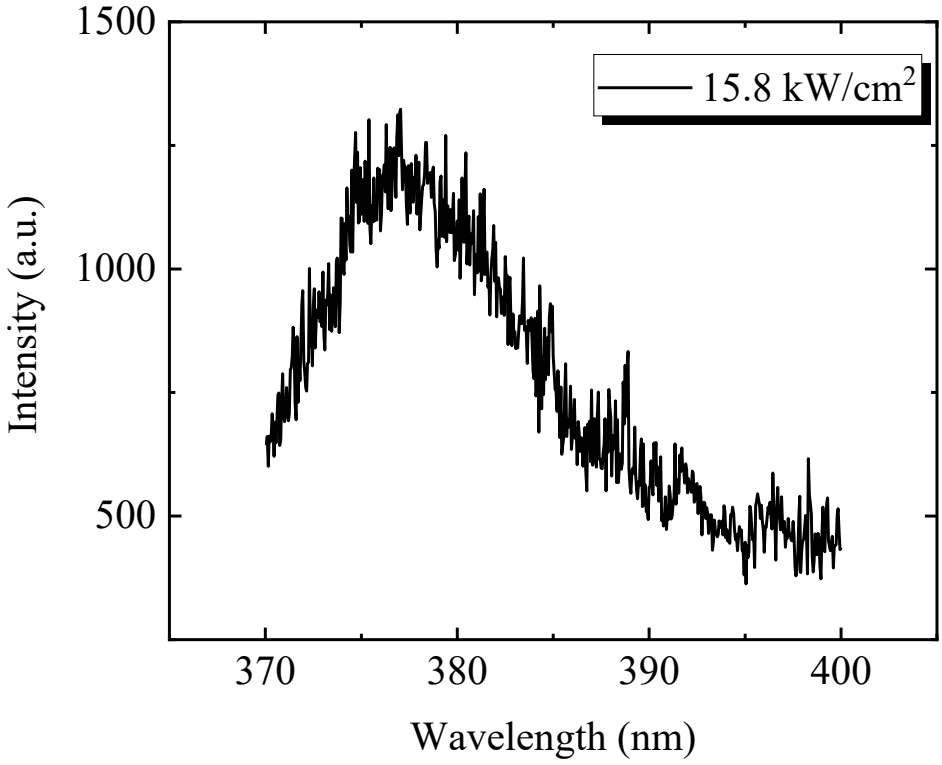

Figure 50. Data collected through a fiber optic cable from a 450 μm diameter disk.

Pumped by the Kimmon Laser.

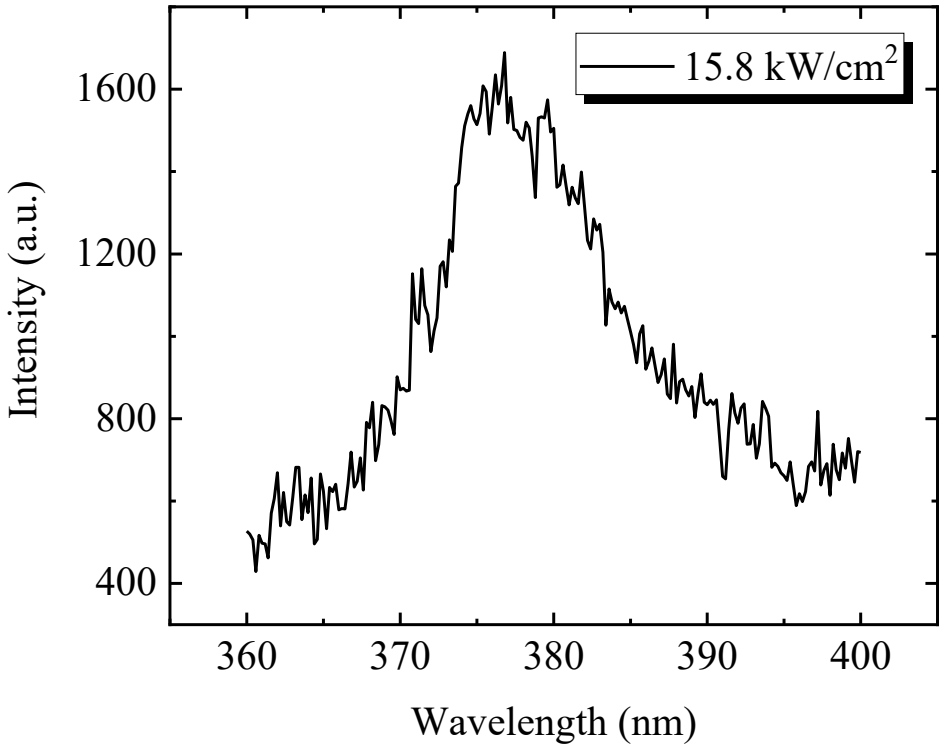

Figure 51. Data collected through a fiber optic cable from a 400 μm diameter disk.

Pumped by the Kimmon Laser.

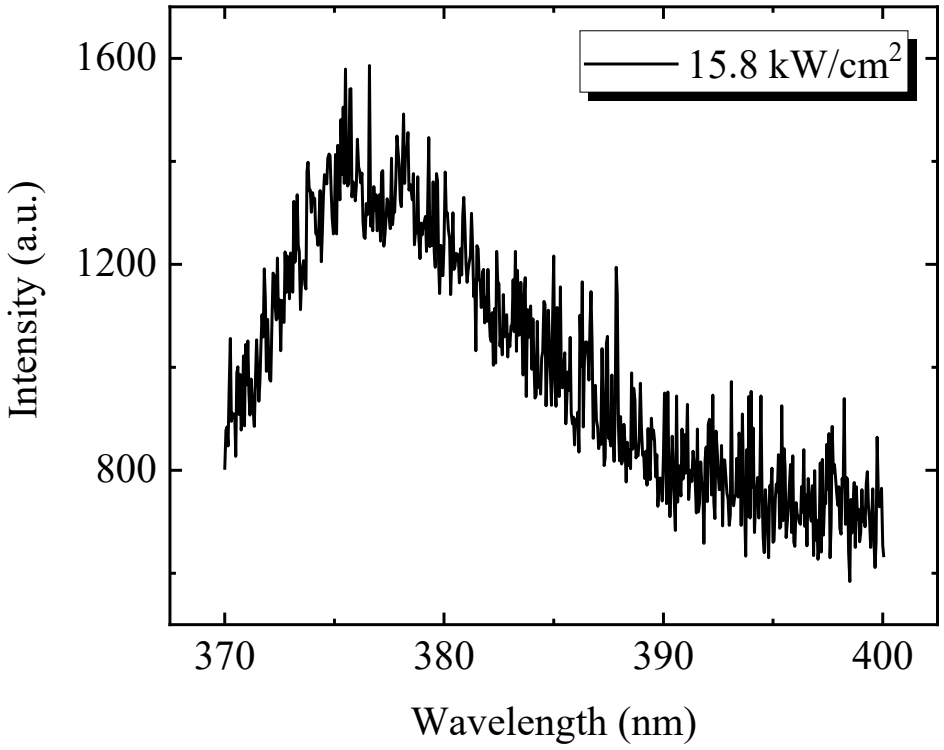

Figure 52. Data collected through a fiber optic cable from a 350 μm diameter disk.

Pumped by the Kimmon Laser.

Appendix B: MATLAB Code

```
%% Power Stored in a WGM. %%

p0 = 1; %normailzed power amplitude

lam0 = 325e-9; %resonnance wavelength
f0 = (2.99e8)./lam0; %resonance frequency
w0 = 2.*pi.*f0; %resonance rad frequency found at 325nm wavelength

Q = [10^3, 10^4, 10^5]; %quality factors (Q-factor) being studied

delwFWHM = w0./Q; %linewidth of frequency,

lam = 300e-9:1e-9:350e-9; %wavelenght range
f = (2.99e8)./lam; %frequency range
w = 2.*pi.*f; % rad frequency range

% graph the power stored in the WGM for each delwFWHM value which
% corresponds to the Q factor of interest.
for x=1:3
   Pw = 1-(p0.*(((delwFWHM(x)./2).^2)./(((w -
w0).^2)+(delwFWHM(x)./2).^2)));

   figure
   plot(w,Pw,'LineWidth',2)
   xlabel('Radian Frequncy')
   ylabel('Normalized Power')
end
```

References

[1] M. Okruss, R. Müller, and A. Hese, "High-resolution UV laser spectroscopy of jet-cooled benzene molecules: Complete rotational analysis of the S1 ← S0 601 (1 = ±1) band," *J. Mol. Spectrosc.*, vol. 193, no. 2, pp. 293–305, 1999, doi: 10.1006/jmsp.1998.7742.

[2] R. M. Silver, J. E. Potzick, and J. Y. Hu, "Metrology with the ultraviolet scanning transmission microscope," *Integr. Circuit Metrol. Insp. Process Control IX*, vol. 2439, no. May 1995, p. 437, 1995, doi: 10.1117/12.209228.

[3] M. Wurm, J. Endres, J. Probst, M. Schoengen, A. Diener, and B. Bodermann, "Metrology of nanoscale grating structures by UV scatterometry," *Opt. Express*, vol. 25, no. 3, p. 2460, 2017, doi: 10.1364/oe.25.002460.

[4] A. Emadi *et al.*, "An UV linear variable optical filter-based micro-spectrometer," *Procedia Eng.*, vol. 5, pp. 416–419, 2010, doi: 10.1016/j.proeng.2010.09.135.

[5] Lord Rayleigh, " CXII. The problem of the whispering gallery ," *London, Edinburgh, Dublin Philos. Mag. J. Sci.*, vol. 20, no. 120, pp. 1001–1004, 1910, doi: 10.1080/14786441008636993.

[6] V. D. Ta, R. Chen, and H. Sun, "Coupled polymer microfiber lasers for single mode operation and enhanced refractive index sensing," *Adv. Opt. Mater.*, vol. 2, no. 3, pp. 220–225, 2014, doi: 10.1002/adom.201300433.

[7] J. Ku *et al.*, "Photonic-Molecule Single-Mode Laser," vol. 27, no. 11, pp. 1157–1160, 2015.

[8] L. Shang, L. Liu, and L. Xu, "Single-frequency coupled asymmetric microcavity laser," *Opt. Lett.*, vol. 33, no. 10, p. 1150, 2008, doi: 10.1364/ol.33.001150.

[9] H. Chandrahalim, S. C. Rand, and X. Fan, “Evanescent coupling between refillable ring resonators and laser-inscribed optical waveguides,” *Appl. Opt.*, vol. 56, no. 16, p. 4750, 2017, doi: 10.1364/ao.56.004750.

[10] H. Chandrahalim and X. Fan, “Reconfigurable Solid-state Dye-doped Polymer Ring Resonator Lasers,” *Sci. Rep.*, vol. 5, no. October, pp. 1–8, 2015, doi: 10.1038/srep18310.

[11] “AFOSR - Physical Sciences.” [Online]. Available: https://www.afrl.af.mil/About-Us/Fact-Sheets/Fact-Sheet-Display/Article/2282129/afosr-physical-sciences/.

[12] “AFOSR - Engineering and Complex Systems.” [Online]. Available: https://www.afrl.af.mil/About-Us/Fact-Sheets/Fact-Sheet-Display/Article/2282117/afosr-engineering-and-complex-systems/.

[13] “AFOSR - Chemistry and Biological Sciences.” [Online]. Available: https://www.afrl.af.mil/About-Us/Fact-Sheets/Fact-Sheet-Display/Article/2282132/afosr-chemistry-and-biological-sciences/.

[14] W. Pongruengkiat and S. Pechprasarn, “Whispering-gallery mode resonators for detecting cancer,” *Sensors (Switzerland)*, vol. 17, no. 9, 2017, doi: 10.3390/s17092095.

[15] S. Soria, *Advanced Sensing with Resonators*, no. May 2019. 2017.

[16] A. Gizatulin and A. Sultanov, “Application of whispering gallery modes (WGM) in optical communications,” no. June 2018, p. 22, 2018, doi: 10.1117/12.2317739.

[17] G. C. Righini *et al.*, “Whispering Gallery Mode microresonators: Fundamentals and applications,” *Riv. del Nuovo Cim.*, vol. 34, no. 7, pp. 435–488, 2011, doi: 10.1393/ncr/i2011-10067-2.

[18] D. G. Rabus and C. Sada, “Ring Resonators: Theory and Modeling,” *Springer Ser. Opt. Sci.*, vol. 127, pp. 3–46, 2020, doi: 10.1007/978-3-030-60131-7_2.

[19] X. Zhang, L. Ren, X. Wu, H. Li, L. Liu, and L. Xu, “Coupled optofluidic ring laser for ultrahigh- sensitive sensing,” *Opt. Express*, vol. 19, no. 22, p. 22242, 2011, doi: 10.1364/oe.19.022242.

[20] W. Lee, H. Li, J. D. Suter, K. Reddy, Y. Sun, and X. Fan, “Tunable single mode lasing from an on-chip optofluidic ring resonator laser,” *Appl. Phys. Lett.*, vol. 98, no. 6, pp. 2011–2014, 2011, doi: 10.1063/1.3554362.

[21] M. L. Gorodetsky, A. D. Pryamikov, and V. S. Ilchenko, “Rayleigh scattering in high-Q microspheres,” *J. Opt. Soc. Am. B*, vol. 17, no. 6, p. 1051, 2000, doi: 10.1364/josab.17.001051.

[22] X. Fan and I. M. White, “Optofluidic microsystems for chemical and biological analysis,” *Nat. Photonics*, vol. 5, no. 10, pp. 591–597, 2011, doi: 10.1038/nphoton.2011.206.

[23] Z. Li, Z. Zhang, A. Scherer, and D. Psaltis, “Mechanically tunable optofluidic distributed feedback dye laser,” in *2006 Digest of the LEOS Summer Topical Meetings*, 2006, pp. 58–59, doi: 10.1109/LEOSST.2006.1693980.

[24] Y. Chen, Z. Li, Z. Zhang, D. Psaltis, and A. Scherer, “Nanoimprinted circular grating distributed feedback dye laser,” *Appl. Phys. Lett.*, vol. 91, no. 5, p. 51109, Jul. 2007, doi: 10.1063/1.2757600.

[25] W. Song, A. E. Vasdekis, Z. Li, and D. Psaltis, “Optofluidic evanescent dye laser based on a distributed feedback circular grating,” *Appl. Phys. Lett.*, vol. 94, no. 16, p. 161110, Apr. 2009, doi: 10.1063/1.3124652.

[26] C. Vannahme, C. L. C. Smith, M. Brøkner Christiansen, and A. Kristensen, "Emission wavelength of multilayer distributed feedback dye lasers," *Appl. Phys. Lett.*, vol. 101, no. 15, p. 151123, 2012, doi: 10.1063/1.4759131.

[27] T. Wienhold *et al.*, "Diffusion driven optofluidic dye lasers encapsulated into polymer chips," *Lab Chip*, vol. 12, no. 19, pp. 3734–3739, 2012, doi: 10.1039/C2LC40494J.

[28] H. Chandrahalim, Q. Chen, A. A. Said, M. Dugan, and X. Fan, "Monolithic optofluidic ring resonator lasers created by femtosecond laser nanofabrication," *Lab Chip*, vol. 15, no. 10, pp. 2335–2340, 2015, doi: 10.1039/c5lc00254k.

[29] G. Aubry, S. Meance, A.-M. Haghiri-Gosnet, and Q. Kou, "Flow rate based control of wavelength emission in a multicolor microfluidic dye laser," *Microelectron. Eng. - MICROELECTRON ENG*, vol. 87, pp. 765–768, May 2010, doi: 10.1016/j.mee.2009.11.130.

[30] Q. Kou, I. Yesilyurt, and Y. Chen, "Collinear dual-color laser emission from a microfluidic dye laser," *Appl. Phys. Lett.*, vol. 88, no. 9, p. 91101, Feb. 2006, doi: 10.1063/1.2179609.

[31] G. Aubry *et al.*, "A multicolor microfluidic droplet dye laser with single mode emission," *Appl. Phys. Lett.*, vol. 98, no. 11, p. 111111, Mar. 2011, doi: 10.1063/1.3565242.

[32] Q. Kou, I. Yesilyurt, G. Escalier, J. C. Galas, L. Coureau, and Y. Chen, "Microfluidic dye laser integration in a lab-on-a-chip device," in *Proc.SPIE*, 2004, vol. 5641, doi: 10.1117/12.576780.

[33] B. Zhen *et al.*, "Enabling enhanced emission and low-threshold lasing of organic

molecules using special Fano resonances of macroscopic photonic crystals," *Proc. Natl. Acad. Sci.*, vol. 110, no. 34, pp. 13711–13716, 2013, doi: 10.1073/pnas.1311866110.

[34] J. Lee *et al.*, "Observation and Differentiation of Unique High-Q Optical Resonances Near Zero Wave Vector in Macroscopic Photonic Crystal Slabs," *Phys. Rev. Lett.*, vol. 109, no. 6, p. 67401, Aug. 2012, doi: 10.1103/PhysRevLett.109.067401.

[35] N. Toropov, G. Cabello, M. P. Serrano, R. R. Gutha, M. Rafti, and F. Vollmer, "Review of biosensing with whispering-gallery mode lasers," *Light Sci. Appl.*, vol. 10, no. 1, 2021, doi: 10.1038/s41377-021-00471-3.

[36] Z. Yuan, Z. Wang, P. Guan, X. Wu, and Y.-C. Chen, "Lasing-Encoded Microsensor Driven by Interfacial Cavity Resonance Energy Transfer," *Adv. Opt. Mater.*, vol. 8, no. 7, p. 1901596, 2020, doi: https://doi.org/10.1002/adom.201901596.

[37] J. Yang and L. J. Guo, "Optical sensors based on active microcavities," *IEEE J. Sel. Top. Quantum Electron.*, vol. 12, no. 1, pp. 143–147, 2006, doi: 10.1109/JSTQE.2005.862953.

[38] Z. Wang *et al.*, "Bio-electrostatic sensitive droplet lasers for molecular detection," *Nanoscale Adv.*, vol. 2, no. 7, pp. 2713–2719, 2020, doi: 10.1039/D0NA00107D.

[39] Y.-C. Chen, Q. Chen, and X. Fan, "Lasing in blood," *Optica*, vol. 3, no. 8, pp. 809–815, Aug. 2016, doi: 10.1364/OPTICA.3.000809.

[40] Y. Sun, S. I. Shopova, C.-S. Wu, S. Arnold, and X. Fan, "Bioinspired optofluidic FRET lasers via DNA scaffolds," *Proc. Natl. Acad. Sci.*, vol. 107, no. 37, pp.

16039–16042, 2010, doi: 10.1073/pnas.1003581107.

[41] U. Bog *et al.*, “Densely Packed Microgoblet Laser Pairs for Cross-Referenced Biomolecular Detection.,” *Adv. Sci. (Weinheim, Baden-Wurttemberg, Ger.*, vol. 2, no. 10, p. 1500066, Oct. 2015, doi: 10.1002/advs.201500066.

[42] T. Wienhold *et al.*, “All-polymer photonic sensing platform based on whispering-gallery mode microgoblet lasers,” *Lab Chip*, vol. 15, no. 18, pp. 3800–3806, 2015, doi: 10.1039/C5LC00670H.

[43] U. Bog *et al.*, “Large-Scale Parallel Surface Functionalization of Goblet-type Whispering Gallery Mode Microcavity Arrays for Biosensing Applications,” *Small*, vol. 10, no. 19, pp. 3863–3868, 2014, doi: https://doi.org/10.1002/smll.201400813.

[44] M. Kuwata-Gonokami *et al.*, “Polymer microdisk and microring lasers,” *Opt. Lett.*, vol. 20, pp. 2093–2095, 1995, doi: 10.1364/OL.20.002093.

[45] S.-Y. Lu *et al.*, “Highly Stable On-Chip Embedded Organic Whispering Gallery Mode Lasers,” *J. Light. Technol.*, vol. 32, no. 13, pp. 2415–2419, 2014, doi: 10.1109/JLT.2014.2326429.

[46] M. Berggren, A. Dodabalapur, and R. E. Slusher, “Stimulated emission and lasing in dye-doped organic thin films with Forster transfer,” *Appl. Phys. Lett.*, vol. 71, no. 16, pp. 2230–2232, 1997, doi: 10.1063/1.120065.

[47] J.-F. Ku *et al.*, “Photonic-Molecule Single-Mode Laser,” *IEEE Photonics Technol. Lett.*, vol. 27, no. 11, pp. 1157–1160, 2015, doi: 10.1109/LPT.2015.2413052.

[48] S. I. Shopova, H. Zhou, X. Fan, and P. Zhang, “Optofluidic ring resonator based dye laser,” *Appl. Phys. Lett.*, vol. 90, no. 22, p. 221101, 2007, doi:

10.1063/1.2743884.

[49] Y. Sun, J. D. Suter, and X. Fan, “Robust integrated optofluidic-ring-resonator dye lasers,” *Opt. Lett.*, vol. 34, no. 7, pp. 1042–1044, Apr. 2009, doi: 10.1364/OL.34.001042.

[50] J. C. Knight, H. S. T. Driver, R. J. Hutcheon, and G. N. Robertson, “Core-resonance capillary-fiber whispering-gallery-mode laser,” *Opt. Lett.*, vol. 17, no. 18, pp. 1280–1282, Sep. 1992, doi: 10.1364/OL.17.001280.

[51] X. Jiang, Q. Song, L. Xu, J. Fu, and L. Tong, “Microfiber knot dye laser based on the evanescent-wave-coupled gain,” *Appl. Phys. Lett.*, vol. 90, no. 23, p. 233501, 2007, doi: 10.1063/1.2746935.

[52] H.-M. Tzeng, K. F. Wall, M. B. Long, and R. K. Chang, “Laser emission from individual droplets at wavelengths corresponding to morphology-dependent resonances,” *Opt. Lett.*, vol. 9, no. 11, pp. 499–501, Nov. 1984, doi: 10.1364/OL.9.000499.

[53] J. C. Galas, J. Torres, M. Belotti, Q. Kou, and Y. Chen, “Microfluidic tunable dye laser with integrated mixer and ring resonator,” *Appl. Phys. Lett.*, vol. 86, no. 26, p. 264101, 2005, doi: 10.1063/1.1968421.

[54] J. D. Suter, W. Lee, D. J. Howard, E. Hoppmann, I. M. White, and X. Fan, “Demonstration of the coupling of optofluidic ring resonator lasers with liquid waveguides,” *Opt. Lett.*, vol. 35, no. 17, pp. 2997–2999, Sep. 2010, doi: 10.1364/OL.35.002997.

[55] Y. Chen *et al.*, “Optofluidic microcavities: Dye-lasers and biosensors,” *Biomicrofluidics*, vol. 4, p. 43002, 2010, doi: 10.1063/1.3499949.

[56] H. Chandrahalim, Q. Chen, A. A. Said, M. Dugan, and X. Fan, "Monolithic optofluidic ring resonator lasers created by femtosecond laser nanofabrication," *Lab Chip*, vol. 15, no. 10, pp. 2335–2340, 2015, doi: 10.1039/C5LC00254K.

[57] M. D. Baaske, M. R. Foreman, and F. Vollmer, "Single-molecule nucleic acid interactions monitored on a label-free microcavity biosensor platform," *Nat. Nanotechnol.*, vol. 9, no. 11, pp. 933–939, 2014, doi: 10.1038/nnano.2014.180.

[58] P. B. Li, S. Y. Gao, and F. L. Li, "Quantum-information transfer with nitrogen-vacancy centers coupled to a whispering-gallery microresonator," *Phys. Rev. A - At. Mol. Opt. Phys.*, vol. 83, no. 5, pp. 3–6, 2011, doi: 10.1103/PhysRevA.83.054306.

[59] M. R. Foreman, J. D. Swaim, and F. Vollmer, "Whispering gallery mode sensors," *Adv. Opt. Photon.*, vol. 7, no. 2, pp. 168–240, Jun. 2015, doi: 10.1364/AOP.7.000168.

[60] Y. P. Rakovich *et al.*, "Whispering gallery mode emission from a composite system of {CdTe} nanocrystals and a spherical microcavity," *Semicond. Sci. Technol.*, vol. 18, no. 11, pp. 914–918, Aug. 2003, doi: 10.1088/0268-1242/18/11/302.

[61] A. N. Oraevsky, M. O. Scully, T. V Sarkisyan, and D. Bandy, "Using whispering gallery modes in semiconductor microdevices," *Laser Phys.*, vol. 9, pp. 990–1003, 1999.

[62] Y. Chu *et al.*, "Lasing of whispering-gallery modes in GaInP waveguide micro-discs and rings with InP quantum dots," *Phys. status solidi c*, vol. 8, no. 2, pp. 325–327, Feb. 2011, doi: https://doi.org/10.1002/pssc.201000537.

[63] V. S. Ilchenko and A. B. Matsko, “Optical resonators with whispering-gallery modes-part II: applications,” *IEEE J. Sel. Top. Quantum Electron.*, vol. 12, no. 1, pp. 15–32, 2006, doi: 10.1109/JSTQE.2005.862943.

[64] J. Lim *et al.*, “Chasing the thermodynamical noise limit in whispering-gallery-mode resonators for ultrastable laser frequency stabilization,” *Nat. Commun.*, vol. 8, no. 1, p. 8, 2017, doi: 10.1038/s41467-017-00021-9.

[65] M. V Maximov *et al.*, “Ultrasmall microdisk and microring lasers based on InAs/InGaAs/GaAs quantum dots,” *Nanoscale Res. Lett.*, vol. 9, no. 1, p. 657, 2014, doi: 10.1186/1556-276X-9-657.

[66] H. Dong, B. Zhou, J. Li, J. Zhan, and L. Zhang, “Ultraviolet lasing behavior in ZnO optical microcavities,” *J. Mater.*, vol. 3, no. 4, pp. 255–266, 2017, doi: 10.1016/j.jmat.2017.06.001.

[67] Q. Zhu, F. Qin, J. Lu, Z. Zhu, Z. Shi, and C. Xu, “Dual-band Fabry-Perot lasing from single ZnO microbelt,” *Opt. Mater. (Amst).*, vol. 60, pp. 366–372, 2016, doi: 10.1016/j.optmat.2016.08.018.

[68] H. Yan *et al.*, “ZnO Nanoribbon Microcavity Lasers,” *Adv. Mater.*, vol. 15, no. 22, pp. 1907–1911, 2003, doi: 10.1002/adma.200305490.

[69] X. Ma, P. Chen, D. Li, Y. Zhang, and D. Yang, “Electrically pumped ZnO film ultraviolet random lasers on silicon substrate,” *Appl. Phys. Lett.*, vol. 91, no. 25, pp. 1–4, 2007, doi: 10.1063/1.2826543.

[70] Y. Chen and Y. Chen, “Enhanced random lasing in ZnO nanocombs assisted by Fabry–Perot resonance,” *Opt. Express*, vol. 19, no. 9, p. 8728, 2011, doi: 10.1364/oe.19.008728.

[71] J. Dai *et al.*, “Combined whispering gallery mode laser from hexagonal ZnO microcavities,” *Appl. Phys. Lett.*, vol. 95, no. 19, pp. 4–7, 2009, doi: 10.1063/1.3264080.

[72] G. Zhu *et al.*, “Different wavelength ranges’ WGM lasing from a ZnO microrod/R6G:PMMA microcavity,” *Epl*, vol. 110, no. 6, 2015, doi: 10.1209/0295-5075/110/67007.

[73] R. Chen, B. Ling, X. W. Sun, and H. D. Sun, “Room temperature excitonic whispering gallery mode lasing from high-quality hexagonal ZnO microdisks,” *Adv. Mater.*, vol. 23, no. 19, pp. 2199–2204, 2011, doi: 10.1002/adma.201100423.

[74] S. Okamoto, Y. Minowa, and M. Ashida, “White-light lasing in ZnO microspheres fabricated by laser ablation,” *Oxide-based Mater. Devices III*, vol. 8263, no. May, p. 82630K, 2012, doi: 10.1117/12.907595.

[75] M. H. Huang *et al.*, “Room-Temperature Ultraviolet Nanowire Nanolasers,” *Science (80-.).*, vol. 292, no. 5523, pp. 1897–1899, 2001, doi: 10.1126/science.1060367.

[76] S. F. Yu, C. Yuen, S. P. Lau, and H. W. Lee, “Zinc oxide thin-film random lasers on silicon substrate,” *Appl. Phys. Lett.*, vol. 84, no. 17, pp. 3244–3246, Apr. 2004, doi: 10.1063/1.1719279.

[77] J. Dai, C. X. XU, K. Zheng, C. G. Lv, and Y. P. Cui, “Whispering gallery-mode lasing in ZnO microrods at room temperature,” *Appl. Phys. Lett.*, vol. 95, no. 24, p. 241110, Dec. 2009, doi: 10.1063/1.3276069.

[78] J. Sun *et al.*, “Realization of controllable etching for ZnO film by NH 4 Cl aqueous solution and its influence on optical and electrical properties,” *Appl. Surf. Sci.*, vol.

253, no. 11, pp. 5161–5165, 2007, doi: 10.1016/j.apsusc.2006.11.036.

[79] T. Zhang, L. Sun, D. Han, Y. Wang, and R. Han, "Surface uniform wet etching of ZnO films and influence of oxygen annealing on etching properties," *NEMS 2011 - 6th IEEE Int. Conf. Nano/Micro Eng. Mol. Syst.*, pp. 626–629, 2011, doi: 10.1109/NEMS.2011.6017433.

[80] J.-M. Liu, *Photonic Devices*. Cambridge University Press, 2005.

[81] H. Yu *et al.*, "ZnO thin films produced by the RF magnetron sputtering," in *Proceedings of 2011 International Conference on Electronic Mechanical Engineering and Information Technology*, 2011, vol. 5, pp. 2486–2489, doi: 10.1109/EMEIT.2011.6023604.

[82] K. Minder *et al.*, "Etching of ZnO toward the development of ZnO homostructure LEDs," in *Zinc Oxide Materials and Devices II*, 2007, vol. 6474, pp. 99–104, doi: 10.1117/12.712784.

[83] G. Nataf, "New approaches to understand conductive and polar domain walls by Raman spectroscopy and low energy electron microscopy," 2016.

[84] Z. K. Tang *et al.*, "Room-temperature ultraviolet laser emission from self-assembled ZnO microcrystallite thin films," *Appl. Phys. Lett.*, vol. 72, no. 25, pp. 3270–3272, 1998, doi: 10.1063/1.121620.

[85] D. Nakamura, T. Simogaki, K. Okazaki, M. Higashihata, H. Ikenoue, and T. Okada, "Synthesis of various sized ZnO microspheres by laser ablation and their lasing characteristics," *J. Laser Micro Nanoeng.*, vol. 8, no. 3, pp. 296–299, 2013, doi: 10.2961/jlmn.2013.03.0018.

[86] H. Dong, B. Zhou, J. Li, J. Zhan, and L. Zhang, "Ultraviolet lasing behavior in

ZnO optical microcavities," *J. Mater.*, vol. 3, no. 4, pp. 255–266, 2017, doi: 10.1016/j.jmat.2017.06.001.

[87] S. Chu, M. Olmedo, Z. Yang, J. Kong, and J. Liu, "Electrically pumped ultraviolet ZnO diode lasers on Si," *Appl. Phys. Lett.*, vol. 93, no. 18, pp. 91–94, 2008, doi: 10.1063/1.3012579.

[88] C. Xu *et al.*, "Whispering-gallery mode lasing in ZnO microcavities," *Laser Photonics Rev.*, vol. 8, no. 4, pp. 469–494, 2014, doi: 10.1002/lpor.201300127.

[89] D. C. Reynolds, D. C. Look, and B. Jogai, "Optically pumped ultraviolet lasing from ZnO," *Solid State Commun.*, vol. 99, no. 12, pp. 873–875, 1996, doi: https://doi.org/10.1016/0038-1098(96)00340-7.

[90] S. H. Jeong, B. S. Kim, and B. T. Lee, "Photoluminescence dependence of ZnO films grown on Si(100) by radio-frequency magnetron sputtering on the growth ambient," *Appl. Phys. Lett.*, vol. 82, no. 16, pp. 2625–2627, 2003, doi: 10.1063/1.1568543.

[91] E. Przeździecka *et al.*, "Photoluminescence, electrical and structural properties of ZnO films, grown by ALD at low temperature," *Semicond. Sci. Technol.*, vol. 24, no. 10, 2009, doi: 10.1088/0268-1242/24/10/105014.

[92] D. W. Hamby, D. A. Lucca, M. J. Klopfstein, and G. Cantwell, "Temperature dependent exciton photoluminescence of bulk ZnO," *J. Appl. Phys.*, vol. 93, no. 6, pp. 3214–3217, 2003, doi: 10.1063/1.1545157.

REPORT DOCUMENTATION PAGE

Form Approved
OMB No. 074-0188

1. REPORT DATE *(DD-MM-YYYY)*	2. REPORT TYPE	3. DATES COVERED *(From – To)*
17-06-2021	Master's Thesis	September 2019 – June 2021

TITLE AND SUBTITLE

Design and Fabrication of Zinc Oxide Optofluidic Laser Elements

5a. CONTRACT NUMBER

5b. GRANT NUMBER

5c. PROGRAM ELEMENT NUMBER

6. AUTHOR(S)

Bodily, Kyle T., Captain, USSF

5d. PROJECT NUMBER

5e. TASK NUMBER

5f. WORK UNIT NUMBER

7. PERFORMING ORGANIZATION NAMES(S) AND ADDRESS(S)
Air Force Institute of Technology
Graduate School of Engineering and Management (AFIT/EN)
2950 Hobson Way, Building 640
WPAFB OH 45433-8865

8. PERFORMING ORGANIZATION REPORT NUMBER

AFIT-ENG-MS-21-J-004

9. SPONSORING/MONITORING AGENCY NAME(S) AND ADDRESS(ES)
AGENCY
ADDRESS
PHONE and EMAIL
ATTN: POC

Intentionally left blank

10. SPONSOR/MONITOR'S ACRONYM(S)

AFRL/RHIQ (example)

11. SPONSOR/MONITOR'S REPORT NUMBER(S)

12. DISTRIBUTION/AVAILABILITY STATEMENT
Distribution Statement A. Approved for Public Release; Distribution Unlimited

13. SUPPLEMENTARY NOTES
This material is declared a work of the U.S. Government and is not subject to copyright protection in the United States.

14. ABSTRACT

This thesis systematically goes through the derivation, simulation, and experimentation of Zinc Oxide optofluidic micro laser elements. Single and coupled ring resonators were simulated to show single mode transmission as well as enhanced coupling capabilities when surrounded by high refractive index liquid. Devices with diameters ranging from 100 – 500 μm were successfully fabricated inexpensively through standard cleanroom procedures. The devices were tested using two different pump laser systems. Testing included such factors as high pump intensity, various angles of excitation, and low temperature. In all cases PL emission was observed and recorded.

15. SUBJECT TERMS
WGM, Laser, Optofluidics, Zinc Oxide

16. SECURITY CLASSIFICATION OF:			17. LIMITATION OF ABSTRACT	18. NUMBER OF PAGES	19a. NAME OF RESPONSIBLE PERSON
a. REPORT	b. ABSTRACT	c. THIS PAGE			Hengky Chandrahalim, AFIT/ENG
U	U	U	UU	110	19b. TELEPHONE NUMBER *(Include area code)* (312) 785-3636, ext 4483 (Hengky.chandrahalim@afit.edu)

Standard Form 298 (Rev. 8-98)
Prescribed by ANSI Std. Z39-18